JOURNAL OF GEOPHYSICAL RESEARCH, VOL. 106, NO. C2, PAGES 2477–2497, FEBRUARY 15, 2001

Turbulence Beneath Sea Ice and Leads: A coupled Sea Ice/Large-Eddy Simulation Study

Eric D. Skyllingstad
College of Oceanic and Atmospheric Sciences, Oregon State University, Corvallis, Oregon

Donald W. Denbo
Joint Institute for the Study of the Atmosphere and Ocean, University of Washington, Seattle, Washington

Abstract. The importance of leads, sea ice motion, and frazil ice on the wintertime ocean boundary layer was examined by using a large-eddy simulation turbulence model coupled to a thermodynamic slab ice model. Coupling was achieved through exchange coefficients that accounted for the differing diffusion rates of heat and salinity. Frazil ice concentrations were modeled by using an ice crystal parameterization with constant crystal size and shape. Stationary ice without leads produced cellular structures similar to atmospheric convection without winds. Ice motion caused this pattern to break down into a series of streaks aligned with the flow. Eddy fluxes were strongly affected by ice motion with relatively larger entrainment fluxes at the mixed layer base under moving ice, whereas stationary ice produced larger fluxes near the top of the boundary layer. Opening of leads caused significant changes in the turbulent structure of the boundary layer. Leads in stationary ice produced concentrated plumes of higher-salinity water beneath the lead. Ice motion caused the lead convection to follow preexisting convective rolls, enhancing the roll circulation salinity and vertical velocity under the lead. Comparison of model time series data with observations from the Arctic Leads Experiment showed general agreement for both pack ice and lead conditions. Simulated heat flux carried by frazil ice had a prominent role in the upper boundary layer, suggesting that frazil ice is important in the heat budget of ice-covered oceans.

1. Introduction

Climate studies consistently point out the importance of polar sea ice as a component in the global heat budget. Major factors that govern ice properties include dynamic processes, which distort the ice causing cracks or leads, and thermodynamic processes, which control freezing and thawing of the ice pack. Because of these processes, significant changes in the heat, salinity, and momentum content of the ocean boundary layer (OBL) are produced as water is exposed in leads or insulated beneath multiyear ice. During the winter, leads are a main conduit for ocean heat loss via radiative, latent and sensible heat fluxes. In the summer, the low albedo of leads allows for significant solar energy flux into the OBL, which forces ice melting at the lead edge and beneath the ice pack. A key parameter in these processes is the turbulent heat transfer between the ice and OBL. This transfer has a dominant role in controlling the sea ice mass budget.

The present study examines how turbulence interacts with ice processes and upper ocean fluxes in the polar ocean. Using a large-eddy simulation (LES) turbulence model coupled with a thermodynamic sea ice model, we focus on freezing conditions under pack ice and leads. Our work is motivated by recent turbulence measurements beneath sea ice and freezing leads [*McPhee* 1992; *McPhee and Stanton*, 1996, hereinafter MS; *Morison and McPhee*, 1998] that have provided a view of the turbulence structure and fluxes in the OBL. By using these observations along with high-resolution model results, we present a detailed picture of turbulence under leads and sea ice with varying ice velocity.

A schematic showing the dominant fluxes that control the ice, heat, and salinity budgets of the upper polar ocean is presented in Figure 1. The most significant drivers of the system are the surface heat and momentum fluxes. Open water in leads and areas of thin ice have the highest upward heat fluxes, which are forced by extremely cold Arctic air masses that are common over the pack ice in winter. These fluxes are compounded by increased longwave radiation flux generated by the relatively warm seawater exposed in the lead. In comparison, heat transfer through thick ice is greatly limited by the insulating properties of the ice and overlying snow cover, which cause relatively low surface temperatures and small values for the latent and sensible heat flux. Because of these factors, fluxes at leads constitute about 1/3 of the total surface heat flux of the Arctic ocean, even though their surface coverage is limited to only a few percent of the ocean [*Maykut*, 1978].

When the motion of sea ice relative to the OBL is small, turbulence beneath leads is forced mainly by convection produced by brine rejection during freezing. Depending on lead size and cooling rates, convection can cause coherent circulations that are linked with the lead geometry, and can transport water directly to the mixed layer base over limited areas [*Morison et al.*, 1992; *Morison and McPhee*, 1998]. Leads

Paper number 1999JC000091.
0148-0227/01/1999JC000091$09.00

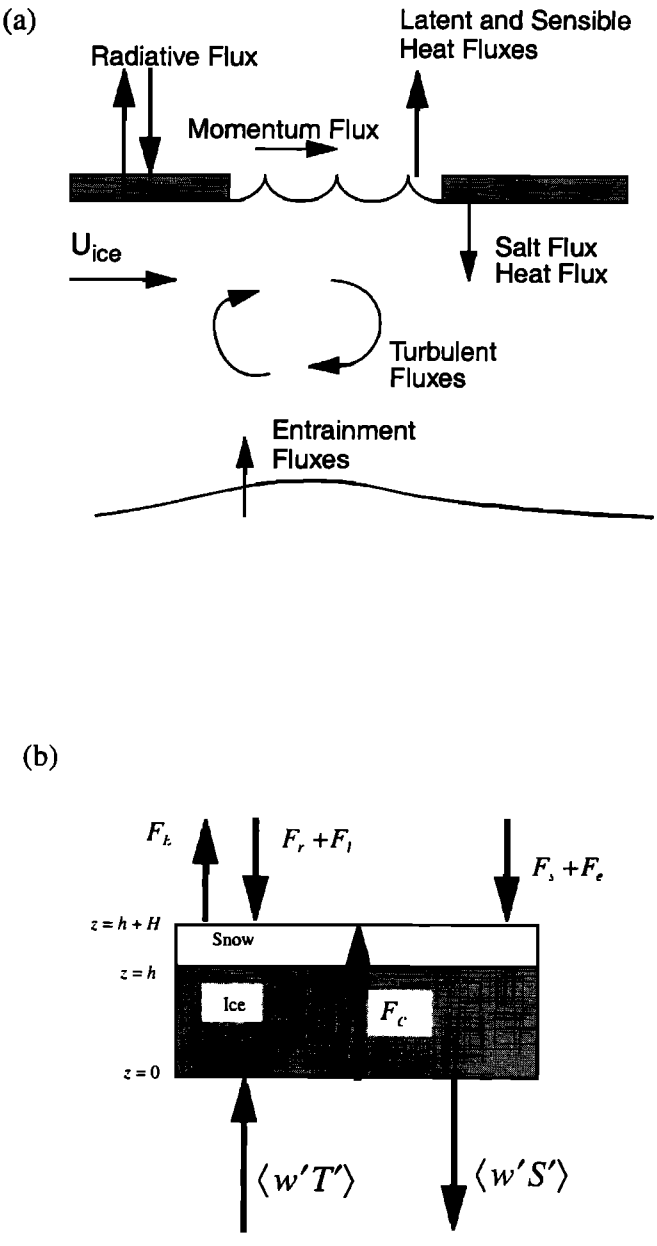

Figure 1. Schematic of the fluxes affecting (a) the ice-covered ocean mixed layer and (b) the ice model. Symbols are defined in the text.

may also cause enhanced upper ocean mixing because of differential momentum flux created as winds impart momentum to the exposed sea surface in the lead and, for larger leads, because of Langmuir circulations generated by wave-current interactions. In contrast to the unique turbulence signature of leads, mixing beneath pack ice is more like an aerodynamically rough wall layer flow. Features in the ice, such as compression ridges, create a turbulent boundary layer that is dependent on the roughness of the ice, ocean current velocities, and the motion of the ice surface. Fluxes of heat and salinity beneath pack ice are much less than the corresponding fluxes under leads because of the reduced surface heat flux and corresponding ice bottom freezing rate and do not typically influence turbulence as much as the bottom roughness [*McPhee,* 1992; MS].

Accurate representation of leads in climate models requires an understanding of how fluxes are distributed laterally beneath leads and sea ice. For example, can leads be parameterized by a mean flux, or do turbulent processes beneath leads require a more sophisticated approach? Critical parameters that control mixing beneath leads are the ice motion and the surface heat flux. Recent measurements by *Morison and McPhee* [1998] and MS demonstrate that the motion of the ice can cause significant variations in the convective circulation beneath the lead and in the salinity flux at the downstream edge of the lead. Two-dimensional turbulence closure modeling studies of mixing processes under leads support these results, showing episodic plume events downstream from the lead in cases with ice motion [*Kantha,* 1995; *Smith and Morison,* 1993, 1998]. While these results are encouraging, they provide only a small sample of the conditions that force turbulence beneath Arctic leads and are unable to yield a detailed three-dimensional analysis of the turbulent processes that occur beneath and downstream from leads.

To extend these results, our approach is to apply a three-dimensional LES model to the problem of convection beneath leads and sea ice. The LES model is coupled with a detailed ice model so that interactions between upper ocean turbulence and sea ice can be directly examined. Our goal is to examine the boundary layer structure created beneath sea ice and leads and determine how ice processes affect turbulence and turbulent fluxes in the under-ice OBL. Using the LES technique, we are able to examine the OBL under slab ice at near-equilibrium conditions. This is not the case with leads, where we can only examine the short-term influence of the lead circulation because of the closed periodic boundaries inherent with LES models.

The paper is organized as follows. A description of the coupled LES-ice model is presented in section 2 along with the experimental design in section 3. Two main experiments are performed by using the model: pack ice and a lead with ice motion. The objective in performing these experiments is to better understand the basic structure and influence of turbulent processes active under sea ice and leads. Key processes that are examined include mixing produced by roughness on the ice pack base, frazil ice, the role of salt flux from ice formation in both leads and under pack ice, and entrainment across the halocline at the mixed layer bottom. Results from these experiments are presented in section 4 including comparisons with flux measurements taken as part of the Arctic Leads Experiment (LEADEX) in spring 1992. The conclusions of the paper are presented in section 5.

2. LES-Ice Model

Most existing ice models focus on the prediction of long-term ice behavior appropriate for climate simulation models. Emphasis has been placed on accurate prediction of ice processes having timescales ranging from days to seasons. As a result, ice processes having very short timescales and spatial scales are usually parameterized. These models include processes, such as heat diffusion through thick ice, that are very slow in comparison with the timescales simulated by using LES (typically 0.5-1 day). One exception is the coupled ice/LES model presented by *Kämpf and Backhaus* [1999] and *Backhaus and Kämpf* [1999], which focuses on sea ice in open ocean conditions over scales considerably larger than the current application.

Because of the limitations of existing models, we decided to build a new ice model based on features from the model of *Cox and Weeks* [1988] and *Maykut* [1978] with parameterizations of ice-water interfaces [*McPhee et al.*, 1987] and frazil ice production [*Omstedt and Svensson*, 1984; *Jenkins and Bombosch*, 1995]. Our goal was to produce an ice model that would accurately predict fluxes of heat and salt between the ocean and ice during either freezing or thawing conditions with an existing ice pack and new ice in leads.

Coupling of the LES model with the slab and frazil ice model is accomplished by the addition of ice-related flux terms to the LES equations. Scalar quantities in the LES were modeled by using

$$\frac{\partial \varphi}{\partial t} = -u_i\frac{\partial \varphi}{\partial x_i} - \frac{\partial}{\partial x_i}\langle u_i''\varphi\rangle + G_\varphi$$

$$\langle u''_i\varphi\rangle = -K_h\frac{\partial \varphi}{\partial x_i}, \quad (1)$$

where φ is temperature T or salinity S; x_i are the Cartesian coordinates with $i = 1$ and 2 denoting the horizontal x and y axis, respectively, and 3 denoting the vertical z axis; u_i are the Cartesian velocity components; t is time; double primes denote subgrid scale quantities that are not explicitly resolved in the flow field; K_h is the scalar eddy diffusivity calculated from the subgrid scale parameterization; and G_φ represents fluxes from frazil ice processes. At the top model grid point adjacent to the ice, the subgrid scale scalar flux, $\langle u_i''\varphi\rangle$, is replaced by the ice bottom temperature and salinity fluxes, $F_{T,S}$, calculated by using the ice model described below.

The equations of motion in the LES model are modified to include the effect of surface ice slab movement and the presence of frazil ice in the water column,

$$\frac{\partial u_i}{\partial t} = -u_j\frac{\partial u_i}{\partial x_j} - \frac{\partial}{\partial x_j}\langle u''_i u''_j\rangle - \frac{\partial \tilde{P}}{\partial x_i} + \varepsilon_{ijk}u_j f_k,$$

$$-\delta_{i3}g\left[\frac{\rho'}{\rho_o} + C\frac{(\rho_o - \rho_i)}{\rho_o}\right] + \alpha\partial^{12}u_i \quad (2)$$

where

$$\langle u''_i u''_j\rangle = -K_m\left(\frac{\partial u_i}{\partial x_j} + \frac{\partial u_j}{\partial x_i}\right); \quad \zeta_k = \varepsilon_{kij}\left(\frac{\partial u_j}{\partial x_i}\right);$$

$$\tilde{P} = \frac{P}{\rho_o} + \frac{2}{3}\overline{q^2};$$

ρ' and ρ_o represent the density perturbation from the initial state and the initial state domain averaged density, respectively; ρ_i is the density of ice; C is the concentration of frazil ice; f_k represents the components of the Coriolis term; g is gravity; P is the pressure; α is a filter factor (applied every 20th time step to remove horizontal $2\Delta x$ noise); K_m is the subgrid scale eddy viscosity; and q represents subgrid scale turbulence kinetic energy (which is combined with pressure and is not explicitly calculated). Frazil ice affects the buoyancy of the water column in the fifth term of the equation. A summary of the LES and ice model constants is presented in Table 1. For a more detailed description of the LES model, we refer the reader to *Skyllingstad et al.* [1999] and *Denbo and Skyllingstad* [1996].

The effects of sea ice roughness on the ocean current structure are parameterized by substituting the under-ice subgrid scale momentum flux at the model top. We apply a Monin-Obukhov similarity profile in estimating the under-ice momentum flux:

$$\langle u_i''u_3''\rangle = C_D\Delta u_i, \quad (3)$$

where

$$C_D = \left[\frac{\kappa}{\ln(\delta z/z_o)}\right]^2,$$

$\Delta u_i = u_{ice} - u_i(z_1)$, $\delta z = 1/2\Delta z$, Δz is the grid spacing, κ is von Kármán's constant, z_o is the ice bottom aerodynamic roughness, and z_1 is the depth of the center of the grid box adjacent to the ice. By using (3), we are implicitly assuming a constant flux over the first grid box in contact with the ice bottom. For cases initialized with constant ice thickness and no leads, the bottom of the ice slab was assumed to be at the model top so that $z_1 = 1/2\Delta z$ (at the first momentum grid point on the staggered Arakawa C grid). This assumption is valid for short simulation periods when the ice growth is relatively minor in comparison with the grid spacing. Leads were treated in the same manner, basically placing the thin lead ice as an upper boundary condition and ignoring dynamic effects associated with the lead edge.

The primary surface fluxes simulated in the surface ice/snow model are shown schematically in Figure 1b. For the snow-covered ice surface, we follow *Cox and Weeks* [1988] and *Maykut* [1978] and calculate the surface temperature, T_o, at each horizontal grid point location by solving an energy balance

$$F_r + F_l - F_E + F_s + F_e + F_c = 0, \quad (4)$$

where

F_r incoming shortwave radiation;
F_l incoming longwave radiation;
F_E emitted longwave radiation;
F_s sensible heat flux;
F_e latent heat flux;
F_c conductive heat flux.

All fluxes have units of watts per square meter. At the ice surface, we prescribe F_r, F_l, and F_e. Emitted longwave radiation is defined by using the Stefan-Boltzman law,

$$F_E = \varepsilon\sigma T_o^4 \quad (5)$$

where ε is the emissivity of ice [*Ebert and Curry*, 1993] and σ is the Stefan-Boltzman constant. Sensible heat flux is parameterized by using a bulk aerodynamic formula:

$$F_s = \rho_a C_p C_s V(T_a - T_o), \quad (6)$$

where ρ_a is the density of air, C_p is the specific heat at constant pressure, C_s is the sensible heat bulk transfer coefficient, V is the wind speed, and T_a is the air temperature. The conductive heat flux is defined by assuming a linear temperature profile through the ice yielding

$$F_c = \frac{k_s k_i}{hk_s + Hk_i}(T_w - T_o), \quad (7)$$

where k_i (W m^{-1} K^{-1}) is the thermal conductivity of the ice [*Maykut*, 1978] defined as

Table 1. Model Constants

	Constant	Value	Unit
α	numerical filter factor	0.5	
g	gravity	9.81	m s^{-2}
ρ_i	ice density	920	kg m^{-3}
κ	von Kármán's constant	0.4	
z_o	ice aerodynamic roughness length	0.03	m
ε	emissivity of ice	0.99	
σ	Stefan-Boltzman constant	5.67 x 10^{-8}	W m^{-2} K^{-1}
ρ_a	density of air	1.4	kg m^{-3}
C_p	specific heat of water	4.217 x 10^3	J (kg °C)$^{-1}$
C_s	sensible heat transfer coefficient	0.003	
k_s	thermal conductivity of snow cover	0.31	W m^{-1} K^{-1}
L	latent heat of fusion	3.34 x 10^5	J kg^{-1}
ν	kinematic viscosity of seawater	1.4 x 10^{-6}	m^2 s^{-1}
α_T	molecular thermal diffusivity of seawater	1.4 x 10^{-7}	m^2 s^{-1}
α_S	molecular haline diffusivity of seawater	7.4 x 10^{-10}	m^2 s^{-1}
Nu	Nusselt number	1.0	
k_w	frazil crystal thermal conductivity	0.564	W m^{-1} °C^{-1}

$$k_i = 2.03 + 0.117\frac{S_i}{T_o},$$

S_i is the ice salinity, k_s is the thermal conductivity of snow cover, h is the ice thickness, H is the snow thickness, and T_w is the temperature of the water at the ice-water interface [*Maykut*, 1978]. The experiments performed in this paper examined conditions with water near or at the seawater freezing point, therefore T_w was prescribed to the freezing temperature, $T_w = -mS_w$, where $m = 0.054$ [*United Nations Educational, Scientific, and Cultural Organization*, 1981], and S_w is the salinity of the water vertically adjacent to the ice. Equations (4)-(7) were solved by using a Newton-Raphson technique to obtain T_O, F_s, F_E, and F_C.

McPhee et al. [1987] developed a set of surface layer flux equations based on a steady state balance between ice melting/freezing and diffusion of heat and salinity. We modified these equations in the present model to include the effects of F_c,

$$w_{ice}Q_L = \langle w_o T_o \rangle - F_c \tag{8}$$

$$w_{ice}(S_w - S_i) = \langle w_o S_o \rangle, \tag{9}$$

where $w_{ice} = -\rho_i/\rho_o d$ represents the vertical velocity of the ice surface (negative with ice growth); $\langle w_o T_o \rangle$ and $\langle w_o S_o \rangle$ represent the heat and salinity flux into the ocean just beneath the ice, respectively; d is the ice growth rate; and $Q_L = L/(C_p\rho_o)$, where L is the latent heat of fusion. Scaling (8) and (9) with the friction velocity $u_* = (\tau/\rho_o)^{1/2}$ and integrating vertically yield

$$\frac{T(z) - T_w}{(w_{ice}Q_L + F_c)/u_*} = \Phi_T \tag{10}$$

$$\frac{S(z) - S_w}{w_{ice}(S_w - S_i)/u_*} = \Phi_S, \tag{11}$$

where τ is the stress imparted by the ice roughness (from (3)) and $T(z)$ and $S(z)$ are the temperature and salinity at the nearest model grid point in the vertical direction (located at z_1).

Knowing u_*, $T(z)$, and $S(z)$ and replacing T_w with $-mS_w$, (10)-(11) describe a quadratic equation for the solution of S_w:

$$mS_w^2 + \left[T(z) - \frac{\Phi_T F_c}{u_*} - mS_i + \frac{\Phi_T Q_L}{\Phi_S}\right]S_w - \left[T(z)S_i - \frac{\Phi_T F_c}{u_*}S_i + \frac{\Phi_T Q_L}{\Phi_S}S(z)\right] = 0, \tag{12}$$

which can then be used to solve for the ice growth velocity

$$w_{ice} = \frac{u_*[S(z) - S_w]}{\Phi_S(S_w - S_i)}. \tag{13}$$

McPhee et al. [1987] point out the significant effect that molecular diffusion has in controlling sea ice melting rates. Because of these possible effects, we implemented the flux model described by *McPhee et al.* [1987]. Nondimensional functions, Φ_T and Φ_S, were prescribed on the basis of the model of *Yaglom and Kader* [1974] as modified by *McPhee et al.* [1987] for the molecular transition sublayer

$$\Phi_{T,S} = \Phi_{\text{turb}} + 1.57\left(\frac{u_* z_o}{\nu}\right)^{\frac{1}{2}}\left(\frac{\nu}{\alpha_{T,S}}\right)^{\frac{2}{3}} \tag{14}$$

$$\Phi_{\text{turb}} = \frac{1}{\kappa}\ln\left(\frac{z}{z_o}\right)$$

where ν is the molecular viscosity and $\alpha_{T,S}$ are the molecular diffusivities of heat and salt, respectively. We follow *Mellor et al.* [1986] in calculating the heat and salinity flux from the ice interface model. Using this approach, fluxes for heat and salinity are defined:

$$F_T = F_c + w_{\text{ice}} Q_L$$

$$F_S = -w_{\text{ice}}(S_i - S(z)). \tag{15}$$

As was shown by Mellor et al., the effects of advection produced by w_{ice} on the heat exchange are negligible in comparison with turbulent wall layer fluxes.

Observed LEADEX upper ocean temperatures were rarely above freezing during the nighttime [see *Levine et al.*, 1993] and as was shown by MS, turbulent heat fluxes at night were usually upward, implying that the seawater adjacent to the ice was supercooled. Supercooled water typically causes frazil ice to form, which releases latent heat, thereby reducing the level of supercooling. We found that applying (13)-(15) without accounting for frazil ice formation produced turbulent heat fluxes near the ice bottom that were much greater than those observed during LEADEX, indicating the need for a frazil ice parameterization. A modified version of the *Omstedt and Svensson* [1984] (hereinafter OS) frazil ice model was employed for this purpose. The original OS model simulates the effects of frazil ice by assuming a concentration of spherical ice crystals having a constant, prescribed radius and rise velocity. Here we modify the OS model by assuming disc-shaped crystals and apply exchange coefficients as defined by Jenkins and Bombosch [1995]. This modification is more consistent with observed crystal shapes; however, as was pointed out by OS, frazil ice can take many forms ranging from hexagonal stars to flat discs.

The modified OS model simulates the growth of frazil through a concentration equation based on the LES scalar equation presented in (1):

$$\frac{\partial C}{\partial t} = -\frac{\partial}{\partial x_i}(u_i C) + \frac{\partial}{\partial x_i}\left(K_h \frac{\partial C}{\partial x_i}\right) + 2Cq(R_i L \rho_i)^{-1} - \frac{\partial}{\partial x_3}(w_r C), \tag{16}$$

where C is the frazil ice concentration, R_i is the prescribed crystal radius, w_r is the ice crystal rise velocity calculated by following *Jenkins and Bombosch* [1995], and q is the source term for freezing and melting. The source term is defined as

$$q = Nu\, k_w \frac{(T_i - T)}{d},$$

where Nu is a Nusselt number; k_w is the thermal conductivity of the ice crystals; T_i is the ice temperature adjacent to the water, taken as the local freezing temperature of the seawater, $T_f = -0.054S - 7.53 \times 10^{-4} z$; T is the local seawater temperature; and d is the crystal disc thickness defined as $0.01R_i$. At the ice slab base, frazil ice is deposited according to the rise velocity flux, $w_r C$. We assume that the subgrid scale flux of frazil ice is equivalent to other scalars, which is reasonable as long as the crystals do not overly affect the local subgrid turbulent velocity field. Freezing and melting of frazil ice affect the temperature and salinity of the water through

$$G_T = \frac{2Cq}{R_i \rho_o C_p}, \quad G_S = \frac{2SCq}{R_i L \rho_o},$$

respectively. As a simplification, we ignore the influence of molecular processes on exchange rates between the crystals and surrounding water.

Our choice of R_i was determined through trial-and-error applications of the ice model using observed turbulent heat and salt fluxes as a basis for validation. Decreasing R_i created greater production of frazil ice but reduced the deposition of frazil on the slab ice via w_r because the rise velocity is proportional to R_i [see *Jenkins and Bombosch*, 1995]. As a result, for small R_i, frazil produced near the ice bottom melted within 2- to 3-m depth because of the pressure dependence of T_f (our initial temperature profile was assumed constant at the under-ice freezing temperature). Melting of frazil produced salt fluxes that were lower than the observations. In contrast, increasing R_i reduced the production of frazil but increased the removal of frazil as w_r increased. On the basis of these test cases, we found that $R_i = 0.001$ m gave results consistent with the observed heat and salt flux behavior observed by MS.

We want to emphasize that the frazil ice model employed in these experiments has not been validated against observations of frazil ice. Many simplifications are contained in this model, such as uniform crystal size, shape, and growth rates. Because of these assumptions, adjustments in the crystal radius and rise velocity were necessary so that the modeled fluxes would match the observed turbulent fluxes. Clearly, a more complete frazil ice model would be preferred, for example, with ice crystal distributions and accurate exchange rates. However, observations of crystal size and shape distributions are needed before such a model can be developed. It is also possible that unforeseen ice processes (e.g., slushy ice) at the ice slab base alter the exchange coefficients defined in (14), thereby preventing supercooling and frazil formation.

Growth and advection of the ice slab were predicted by using the ice growth and rise velocity and prescribed ice advective velocity field, u_{ice} and v_{ice}:

$$\frac{\partial h}{\partial t} = -u_{\text{ice}}\frac{\partial h}{\partial x} - v_{\text{ice}}\frac{\partial h}{\partial y} - \frac{\rho_o}{\rho_i} w_{\text{ice}} + w_r C. \tag{17}$$

Throughout our simulations, u_{ice} was held constant and v_{ice} was set to zero. Leads were initialized with an existing ice

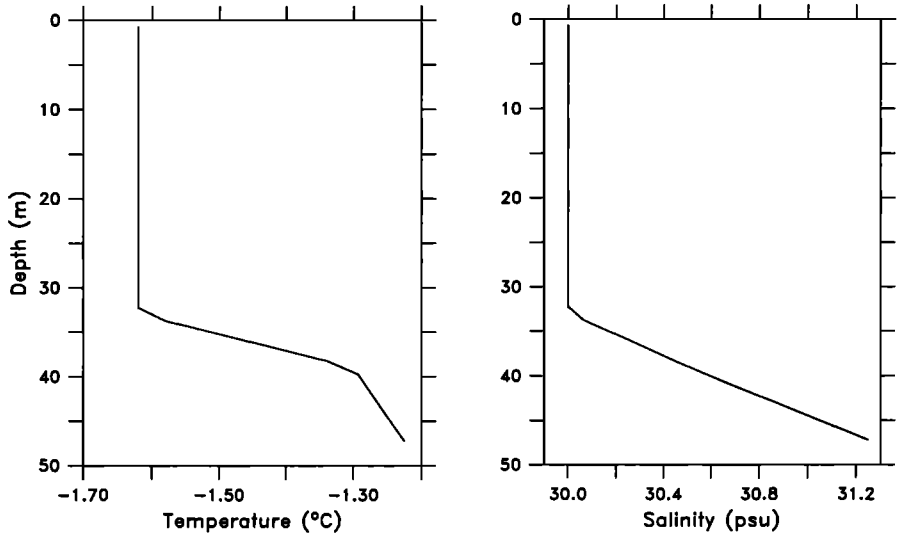

Figure 2. Initial potential temperature and salinity profiles representing conditions during LEADEX.

cover of 0.08 m, to avoid short-term processes involving the transport and rafting of grease ice across the lead.

3. Experimental Design

The main focus of the LES experiments was to quantify the influence of ice motion, brine rejection, and frazil ice on the upper ocean mixed layer. Initial conditions were prescribed by using an idealized neutral boundary layer profile representative of conditions measured during LEADEX (Figure 2). Initial ice thickness was set to 1 m with a snow depth of 0.25 m for pack ice; leads were initially assumed to have ice coverage of 0.08 m without snow cover. Other external forcing parameters were set as follows: F_s = 0 W m^{-2}, F_e = 100 W m^{-2}, F_l = 80 W m^{-2}, T_a = -25°C, and V = 7.4 m s^{-1} (giving a wind stress of ~0.1 N m^{-2}) representing conditions for midwinter at the LEADEX location. Ice salt content, S_i, was set to 4 practical salinity units (psu) for pack ice and 16 psu for thin lead ice, reflecting observations of ice salinity during rapid freezing [*Eicken et al.*, 1998]. Pack ice experiments without leads were performed by using a domain size of 192 m x 192 m in the horizontal and 48 m in the vertical with a grid spacing of 0.75 m (256 x 256 x 64 grid points). For cases with leads, a domain size of 720 m x 720 m in the horizontal and 48 m in the vertical was chosen with a grid spacing of 1.5 m (480 x 480 x 32 grid points). A small (10%) random variability was added to the ice stress and salinity flux during the initial simulated hour to promote the formation of turbulent eddies. Simulations without leads were performed for 12 hours, which is ~6 large-eddy turnover times, to allow for the development of a near steady state boundary layer turbulent structure. Simulations with leads were run for 10 hours before initializing the lead.

Periodic lateral boundary conditions were applied with an open radiative boundary condition from *Klemp and Durran* [1983] at the model base. LES models almost always employ periodic horizontal boundaries to avoid having to define three-dimensional turbulence velocity and scalar fields outside of the model domain. Higher-order closure models such as those used by *Kantha* [1995] or *Mellor et al.* [1986] do not have this restriction because turbulence is completely parameterized and is not resolved as it is in LES. For boundary layers with homogeneous forcing (for example, a uniform ice field), periodic boundaries do not pose a significant problem. However, with leads, circulations set up by the lead surface forcing will cause changes in the boundary layer structure that can ultimately affect the turbulence signature produced by the lead. To avoid this interaction, the duration of lead simulations was limited so that the lead did not significantly change the overall boundary layer structure. The use of period boundaries imposes a significant constraint on the length of lead simulations, limiting our investigation to a few hours following the initial lead opening. We cannot realistically examine the long time period response of the OBL to leads by using the LES method, except for cases with lead coverage equivalent to the experimental setup (~21%), which is considerably higher than observed wintertime lead coverage (~5%) during storms. Instead, we focus on the turbulent structure near the lead and make comparisons with similar observations.

Resolution in the lead simulations was reduced so that the model domain could be increased, thereby permitting longer simulations. Reduced resolution decreases the accuracy of the resolved eddy structure near the upper boundary adjacent to the ice slab, which may cause a problem in comparing our results with turbulence observations taken beneath the ice during LEADEX. These measurements were typically taken at ~4 m below the ice, which is only ~3 grid points in the lead simulations. However, for the heat and salinity flux, most of the vertical transport is achieved through eddies that scale with the mixed layer depth (~32 m), so that subgrid fluxes are still small in comparison with the resolved eddy fluxes (this is shown in our analysis). Nevertheless, details of the turbulent structure adjacent to the ice are necessarily lacking because the flow is dominated by shear and the vertical eddy structure is limited by the grid resolution.

Two methods were considered for simulating ice motion. In the first method, motion was modeled by holding the lead position constant at the center of the model domain and imposing a constant advective velocity for the entire water

Table 2. Experimental Parameters

Experiment	Ice Velocity	Ice Thickness h
No-lead Simulations	U_{ice} = 0.0, 0.03, 0.09, 0.12 m s^{-1}	1 m
150-m lead simulations	U_{ice} = 0.0, 0.03, 0.09 m s^{-1}	pack, 1 m; lead, 0.08 m

column [e.g., *Kantha,* 1995]. The second method held the model domain at a constant position and moved the surface ice field [e.g., *Smith and Morison,* 1998]. Both cases are fundamentally the same because of the periodic boundaries (we are essentially performing a Galilean transformation). However, in the first method, changing the average water velocity generates increased numerical smoothing that is inherent with the flux conserving finite difference methods used to advect scalar quantities. Moving the water also poses a more stringent criterion on the maximum advective time step because the background water velocity is the speed of the ice rather than zero. To avoid these problems, we chose to move the ice and initialize the water velocity at zero.

Lead cases were initialized after a 10-hour spin up period by reducing the ice thickness over a rectangular region centered on the x axis and extending in the y direction across the domain with constant width of 150 m. Simulations were performed for 2 hours after lead initialization, which is about the time it takes for the fastest-moving lead case (0.09 m s^{-1}) to advance across the x axis periodic boundary, reenter the domain on the opposite side, and move back to about the center of the domain.

Results from the Surface Heat Budget of the Arctic Ocean (SHEBA) experiment suggest that the ocean boundary layer and ice move as essentially one unit, rotating with an inertial frequency in response to wind forcing (M. McPhee, personal communication, 1999). Because of this observation, we chose an inertial reference frame for the simulations as was done by *Skyllingstad et al.* [2000]. In this reference frame, the vertical component of the Coriolis term is set to zero, avoiding the inertial rotation of the ice and mean current structure.

4. Results

A series of seven experiments were performed as outlined in Table 2. A range of ice velocities were considered, with maximum values chosen to match observed ice velocities during selected cases from LEADEX. We begin our analysis with an overview of the turbulence structure beneath pack ice without leads.

4.1. No-Lead Simulations: Turbulence Structure, Transport, and Energetics

The first set of simulations represent conditions that might be expected in regions of uniform first-year ice coverage without leads and with minimal dynamic effects such as ridges and keels. Under these conditions, mixing in the upper water column is generated mostly by ice bottom roughness and convection forced by salinity flux as new ice freezes on the bottom of the ice pack. Although the upper ocean fluxes of heat and salinity without leads are relatively small, a large portion of the Arctic ocean has these conditions as an upper boundary during the winter months. Thus turbulent fluxes produced under pack ice are an important part of the overall Arctic ocean salinity and heat budget.

The salinity structure near the top of the OBL is shown in Figure 3 for each of the pack ice velocity scenarios (Table 2) after 12 hours. The ice growth was nearly constant for each case at ~0.0037 m per day from direct freezing and ~0.001 m per day from frazil ice deposition. As new ice forms beneath stationary sea ice (Figure 3a), rejected brine provides the primary forcing for turbulence. Under the ice, convective cells are produced with scales (~50 to 75 m) that are about twice the mixed layer depth. Coherent structures (as shown by animations) appear as narrow downwelling plumes surrounded by broad regions of upwelling, consistent with previous studies of planetary boundary layer convection [*Moeng,* 1984; *Mason,* 1989]. With ice motion, the cellular coherent patterns quickly form into streaky structures that are aligned in the direction of the ice motion (Figures 3b-3c), much like the coherent turbulent structure in the atmospheric boundary layer [see *Moeng and Sullivan,* 1994]. Scale and separation between streaks appear to increase slightly with increasing ice velocity.

Vertical cross sections from cases with U_{ice} = 0.0 m s^{-1} and 0.12 m s^{-1} in Figure 4 show the effect that ice motion has on the transport of salt from the ice base to the upper halocline. When U_{ice} = 0.0 m s^{-1}, plumes transport salt downward with weak lateral mixing (e.g., x = ~80 m). Setting the ice velocity to 0.12 m s^{-1} disrupts the coherence of the salt plumes and generates more concentrated bursts that mix downward in response to local regions of momentum flux from the ice. Plumes actively transport horizontal momentum created by the motion of the surface ice field as shown by the relatively strong positive zonal velocity perturbation in the plume at x = ~10 m. These plumes of enhanced momentum cause increased mixing of halocline water near the mixed layer base, for example, as demonstrated by the detrainment of saltier water at x = ~130, z = 30. The correspondence of high salinity with high momentum flux in the streaks when U_{ice} = 0.12 m s^{-1} is consistent with atmospheric results from *Moeng and Sullivan* [1994] and *Khanna and Brasseur* [1998], who indicate that boundary streaks are regions of high momentum and scalar flux. Overall, the average salinity in Figures 3 and 4 increases slightly when going from U_{ice} = 0.0 m s^{-1} to U_{ice} = 0.12 m s^{-1}. Analysis of the turbulent fluxes (presented below) indicates that entrainment at the mixed layer base causes this increase.

Because of the role convection may have in controlling salt and heat flux at the base of the Arctic ocean boundary layer, we are particularly interested in the vertical penetration of eddies produced at the ice-water interface. One measure of eddy strength is the magnitude of the horizontally averaged eddy salt and heat fluxes, $\overline{w'S'}$, $\overline{w'T'}$, which are key terms in the budgets of the horizontally averaged heat and salt:

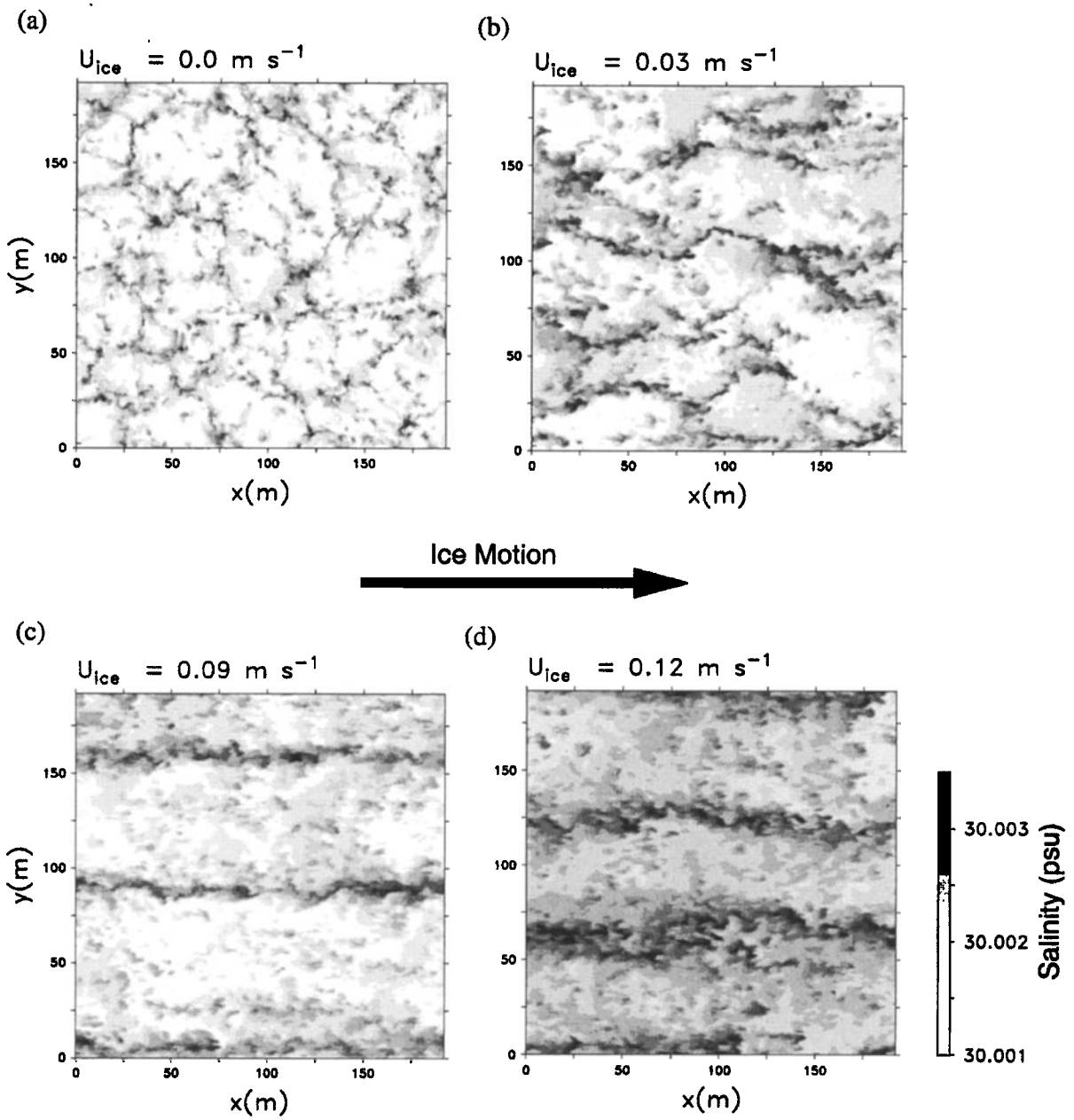

Figure 3. Salinity (psu) at a depth of 4.1 m after 12 hours for ice velocities of (a) 0.0, (b) 0.03, (c) 0.09, and (d) 0.12 m s^{-1}.

$$\frac{\partial}{\partial t}\bar{S} = -\frac{\partial}{\partial z}(\overline{w'S'} + K_h\frac{\partial}{\partial z}\bar{S}) + \bar{G}_s$$

$$\frac{\partial}{\partial t}\bar{T} = -\frac{\partial}{\partial z}(\overline{w'T'} + K_h\frac{\partial}{\partial z}\bar{T}) + \bar{G}_T. \qquad (18)$$

Primes in these equations denote perturbations about the horizontal mean and represent the turbulent eddies, whereas overbars denote horizontal averages or mean profile values. Eddy salt and heat fluxes for the four ice velocities are presented in Figure 5. Also shown are the subgrid scale heat flux, demonstrating that the resolved eddy fluxes are dominant except for very near the surface and in the upper pycnocline at the mixed layer base. Throughout most of the boundary layer, the salt fluxes for each case have similar profiles with a peak downward flux just below the ice at ~2.5 m. Near the bottom of the boundary layer, the U_{ice} = 0.12 m s^{-1} salt flux increases more rapidly so that the upward flux at ~30 m is ~50% higher than the stationary case, indicating greater entrainment of halocline water. This result is consistent with the high momentum pulses noted in Figure 4b, which sweep halocline water upward into the mixed layer. With ice motion, turbulence at the mixed layer base is generated via increased mean current shear. Stronger turbulence produces a greater local flux as saltier halocline water is transported upward. When the ice is stationary, convective cells transport salt directly to the mixed layer base; however, this generates less mixing of water from the

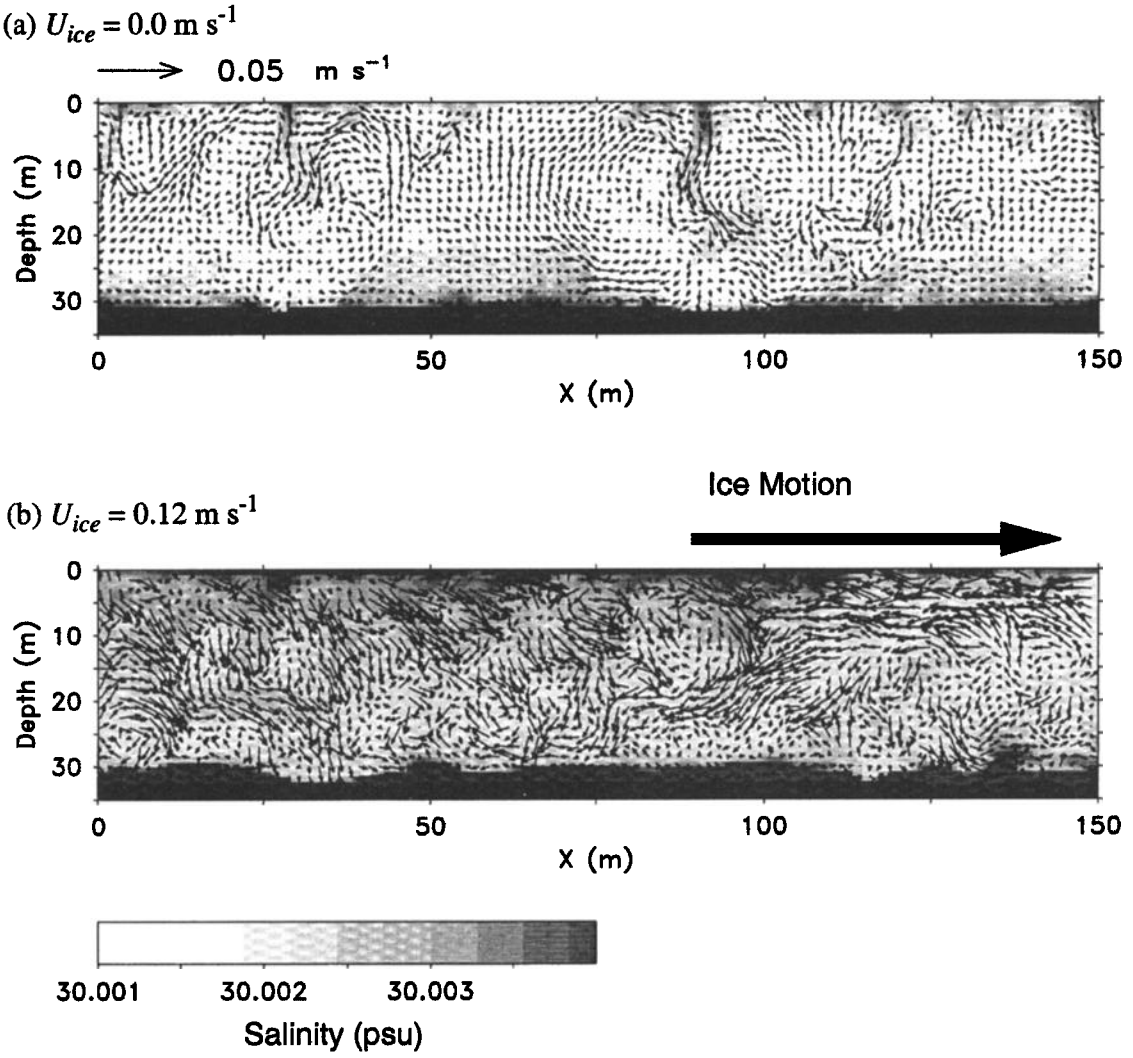

Figure 4. Vertical cross sections of perturbation velocity vector and salinity (psu) at hour 12 from (a) U_{ice} = 0.0 m s^{-1} and (b) U_{ice} = 0.12 m s^{-1}. Cross sections are taken from (a) y = 165 m and (b) y = 5 m. Vectors are plotted for every other grid point.

upper halocline in comparison with shear-generated turbulence. Plots of the turbulent heat flux also demonstrate the effect of shear-induced entrainment, although in the case of heat, the flux divergence is reversed from the salt flux because the ice heat flux is positive.

The evolution of turbulence can be quantified through the budget equation for horizontally averaged turbulence kinetic energy,

$$\frac{\partial E}{\partial t} = \underbrace{-\overline{u_i' u_3'}\frac{\partial \bar{u}_i}{\partial x_3}}_{\text{I}} \underbrace{- \overline{u'_3 \cdot g\frac{\rho'}{\rho_o}}}_{\text{II}} \underbrace{+ \overline{\langle u''_i u''_3 \rangle \frac{\partial u'_i}{\partial x_j}}}_{\text{III}} \underbrace{- \overline{\frac{\partial}{\partial x_3}(u'_3 E + u'_i \langle u''_i u''_3 \rangle + u'_3 \tilde{P})}}_{\text{IV}} \quad (19)$$

where

$$\langle u''_i u''_j \rangle = -K_m\left(\frac{\partial u_i}{\partial x_j} + \frac{\partial u_j}{\partial x_i}\right)$$

and primed quantities again denote the resolved eddy field or departure from the horizontal mean, $E = \langle 1/2\rho u'^2_i \rangle$. Terms in the E budget equation are referred to as (I) shear production, (II) buoyant production, (III) dissipation, and (IV) total vertical transport by resolved eddies, subgrid turbulence, and pressure, respectively. Plots of the dominant terms in are shown in Figure 6 for the four ice velocity cases presented above. With stationary ice, E is produced mainly by buoyancy as saline plumes accelerate away from the ice. Interestingly, frazil formation just below the pack ice causes a negative buoyancy term because of stratification produced by the lower-density frazil. A portion of the turbulence produced near the ice bottom is transported downward by pressure and advective transport, so that dissipation rates ~5 m beneath the ice are somewhat smaller than the buoyancy term. At the mixed layer base, the transported E performs work against the stable stratification of the halocline, as shown by the negative buoyancy production term. Dissipation rates are very uniform with depth showing that the transport and buoyancy terms tend to counteract each other.

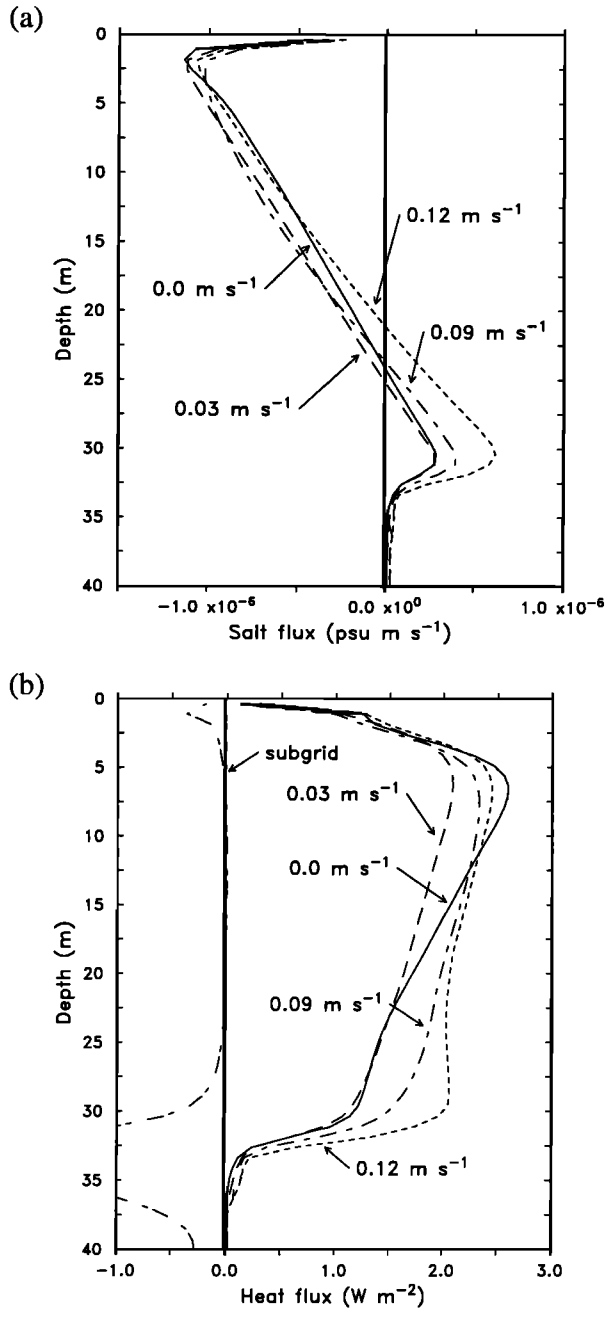

Figure 5. Horizontally averaged (a) salinity flux and (b) heat flux from under-ice simulations with ice velocities of 0.0, 0.06, and 0.12 m s^{-1}.

Ice motion causes significant changes from the stationary E budget, particularly in the upper section of the profile. Current shear generated by the ice creates a shear production term that has two main effects near the ice base. First, the dissipation rate increases so that a large portion of the shear production term is immediately canceled through the subgrid model. The second major effect of the shear is to decrease the relative importance of the buoyancy and advective terms near the surface. Deeper in the water column, however, shear production and the transport of E begin to have a dominant role as ice velocity is increased. When $U_{ice} = 0.12$ m s^{-1}, both the transport and shear production cause significant entrainment at the mixed layer base as shown by the increased buoyancy term at 30-35 m in Figure 6d.

4.2. Comparison With LEADEX Data: No Lead.

Measurements of turbulence parameters during LEADEX provide a unique data set for testing the LES model in simulating under-ice turbulence. Under-ice measurements can be acquired with less difficulty in comparison with open-water measurements because of the relatively stable platform provided by the ice sheet. Time series comparisons are made by using five model profiles that are moving with the ice sheet velocity, representing stations anchored to the ice surface. Initial positions of the model profiles were taken from a depth of ~2.6 m at the $x = 1.5$ m boundary and for five y positions ranging every 22.5 m starting at $y = 1.5$ m. Because the flow is turbulent, we cannot expect to duplicate the exact conditions that were encountered during LEADEX, but we can make qualitative comparisons and establish if the LES model reproduces statistical variability consistent with observed turbulence.

Time series plots of the perturbation temperature, salinity, zonal velocity, vertical velocity, eddy heat, and eddy salt fluxes from a 1-hour period on LEADEX day 85.122 (Runway experiment, MS) are shown in Figure 7 along with simulation results from hour 12 at $y = 24$ m. Perturbations in these plots are calculated by subtracting a linear trend from each time series (this is denoted by the circumflex in the figure) and are therefore slightly different from the perturbation quantities calculated by subtracting the horizontal mean. Model results are taken from the $U_{ice} = 0.12$ m s^{-1} case, which is very close to the observed ice velocity of 0.118 m s^{-1}. Because the observations were made at night (around midnight, local time), we assume that surface forcing was similar to the idealized simulation values, although daytime solar heating and a diurnal cycle in the mixed layer fluxes may have produced a lagged signal in the temperature (see MS for details). The largest qualitative differences between the observations and model results are, for the most part, related to the smoother model time series. Model time series are filtered by the combination of a 4-s model time step, versus 1.5 s for the observations, and temporal averaging of the third-order Adams-Bashforth time-differencing scheme. The LES model fields are also filtered by the subgrid scale parameterization so that the smallest resolved eddies (~$2\Delta x$) have very little energy. In effect, the LES model cannot accurately simulate turbulence with length scales much smaller than $4\Delta x$.

Plots of the eddy fluxes also show the effects of smoothing, with measured data having more pronounced peaks in the fluxes. On average, however, modeled fluxes are within ~20% of the observations, mostly because the large-scale eddies are responsible for the bulk of the scalar transport. Some of this agreement is based on our choice of the frazil ice crystal size, which was selected to yield a heat flux match with the no-lead, Runway experiment data, thus fitting the model to the observations. Many factors could explain the differences between the model and observations, but overall the qualitative comparison is encouraging, especially given that our forcing is only an approximation of the actual data.

A more quantitative comparison of the model and observations can be made by using ensemble-averaged spectra. We computed the ensemble-averaged, observed spectral energy,

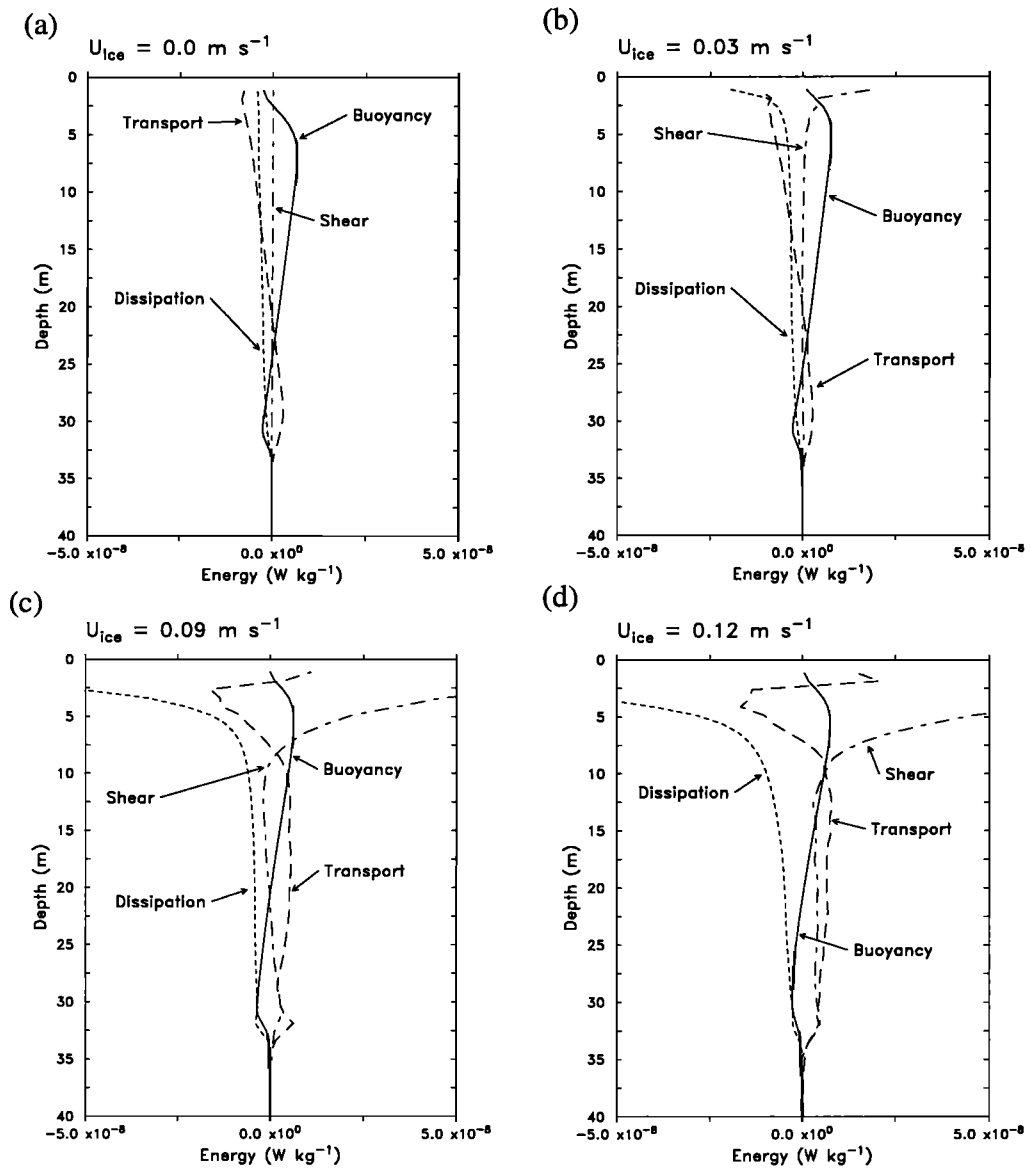

Figure 6. Vertical profiles of the horizontally averaged turbulence kinetic energy budget terms of equation (19) for shear production (I), buoyancy production (II), dissipation rate (III), and total transport (IV) for ice velocities of (a) 0.0 m s^{-1}, (b) 0.03 m s^{-1}, (c) 0.09 m s^{-1}, and (d) 0.12 m s^{-1}.

$S(f)$, where $f = 2\pi/T$, and T is the period, using data from five individual hours ranging over day 85.122 to 85.289 of LEADEX, taken from the "Runway" experiment (Figure 8). The five time periods were selected on the basis of the condition that the net salt flux was negative, indicating freezing conditions at the ice base. Average ice velocities during the time of these measurements were between 0.115 and 0.13 m s^{-1}. Averages from the model were created by using the five time series described above. Model spectra are limited by the grid resolution to a maximum frequency (1/2 the Nyquist frequency) equal to $\pi U/2\Delta x$, where $U = U_{ice} - u(z = 3.4\text{ m}) = \sim 0.08$ m s^{-1} is the ice relative average horizontal velocity at z = 2.6-m depth. As Figure 8 shows, the model compares favorably with the low-frequency flow features and is able to duplicate the -1 spectral behavior that is evident in the measured data. The presence of a -1 spectral region in the measured and model data is consistent with observations of wall-bounded flow reported by *Katul and Parlange* [1995]. *Kader and Yaglom* [1991] refer to this range of frequencies (or wavenumbers) as the "production range," where energy is injected into the turbulence field from the mean shear.

At higher frequencies, the observed spectra follow a -5/3 power law indicating an inertial subrange that extends to the instrument resolution. Turbulence energy at these frequencies is gained or lost primarily through interactions with other turbulent eddies, with little injection of energy from the mean flow. Simulated $S_{ww}(f)$ and $S_{ss}(f)$ have a more limited -5/3 region in comparison with the data because of the model resolution but are in good agreement at the resolved frequency. The agreement between the model and observed spectra to just beyond the observed transition between the -1 and -5/3 regions indicates that the model resolution is likely sufficient

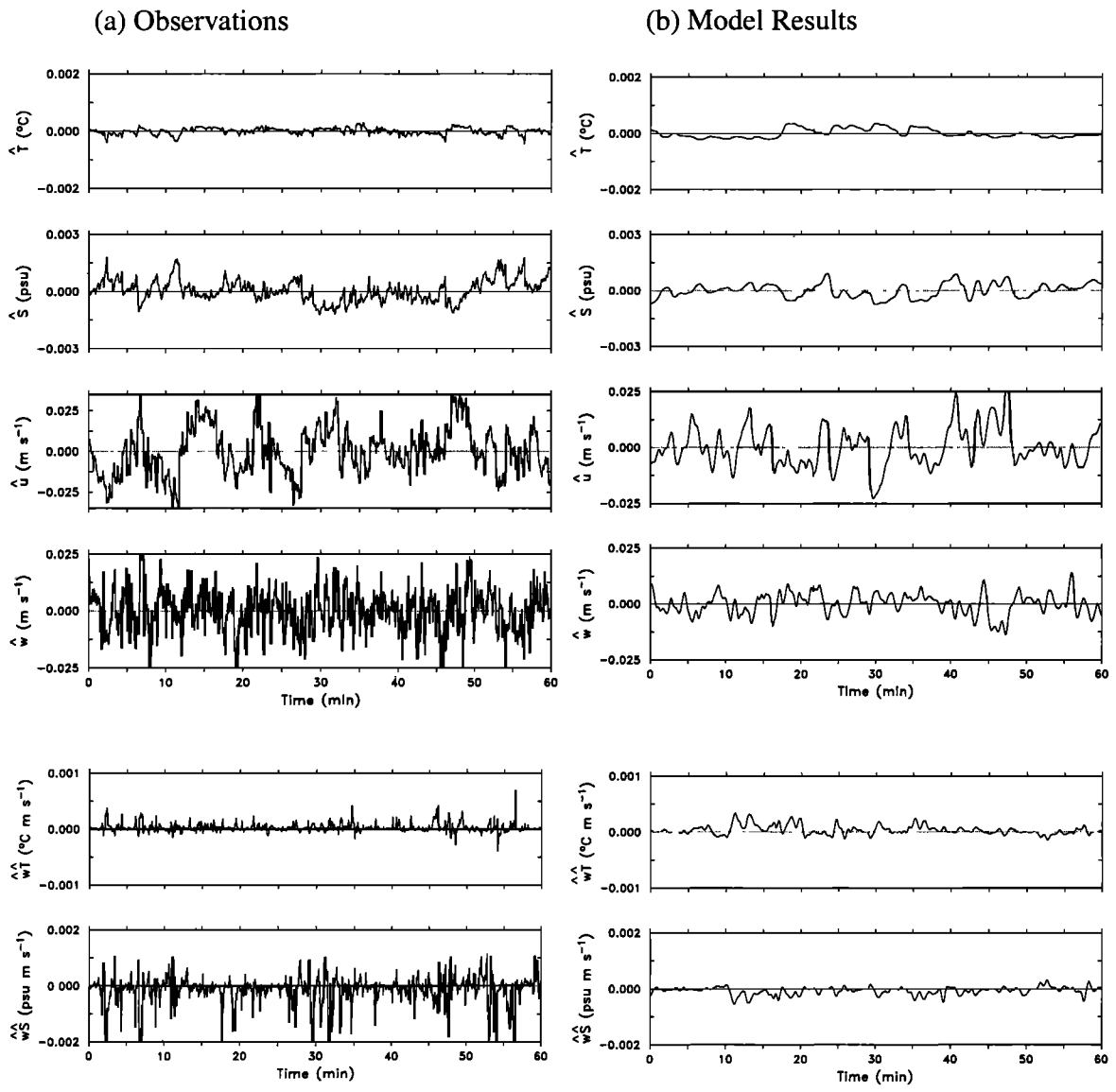

Figure 7. Time series of (a) observed and (b) modeled perturbation temperature, perturbation salinity, perturbation zonal velocity, vertical velocity, heat flux, and salt flux. Observations are taken starting at day 85.122 of LEADEX from a depth of 3.0 m below the ice. Model results are from $y = 24$ m between hours 11 and 12 at a depth of 2.625 m. The average observed heat and salinity fluxes are 2.81 x 10^{-7} K m^{-2} (1.14 W m^{-2}) and -1.63 x 10^{-6} psu m s^{-1}, where the average modeled heat and salinity fluxes are 2.0 x 10^{-7} K m^{-2} (0.8 W m^{-2}) and -1.11 x 10^{-6} psu m s^{-1} (from five time series adjusted to 3-m depth).

for the current application. Further confidence is provided by the spatial spectra, taken as the x axis ensemble average of the y axis spectra, which indicate a broader -5/3 region in the model spectra.

4.3. Lead Simulations: Turbulence Structure, Transport, and Energetics

The lead experiments focus on three different ice velocity cases, each having identical forcing as the no-lead cases but with different surface ice velocities as shown in Table 1. Lead simulations are performed by initializing the flow fields as in the uniform ice simulations discussed above and then at hour 10 opening a 150-m-wide lead extending across the y direction, centered on the x axis (see the $U_{ice} = 0.0$ case in Figure 9 for the approximate initial location). We chose this initialization procedure so that turbulence in the boundary layer would be fully developed, simulating upper ocean conditions after a sustained period under uniformly rough ice before encountering the lead. Initial ice thickness of the lead was set to 0.08 m, which yielded a nearly constant ice growth rate of ~0.028 m/d over the lead during the 2-hour simulation period.

Horizontal cross-section plots of the salinity for the lead cases are shown in Figure 9 from a depth of 3.8 m at hour 12 or 2 hours after initializing the lead. As in the no-lead cases, ice motion has a profound effect on the strength and organization of turbulence in the boundary layer. When ice is stationary, plumes are produced at the lead edge that quickly

remove the more saline water produced during freezing at the lead surface and transport it to the mixed layer base. The structure of turbulence in this case is almost completely determined by the lead cooling rate and lead width, with convective plumes acting as a conduit for the vertical transport of salt and heat. Because the lead is considerably wider than the mixed layer depth, the pattern of convection is dominated by two regions of downward motion, rather than a single plume centered on the lead axis. This is shown more clearly in a vertical cross-section plot (Figure 10a), where two regions of strong vertical motion are indicated ~50 m apart in the center of the lead.

Ice motion breaks the symmetry of the lead convective circulation by disconnecting the surface forcing from the rest of

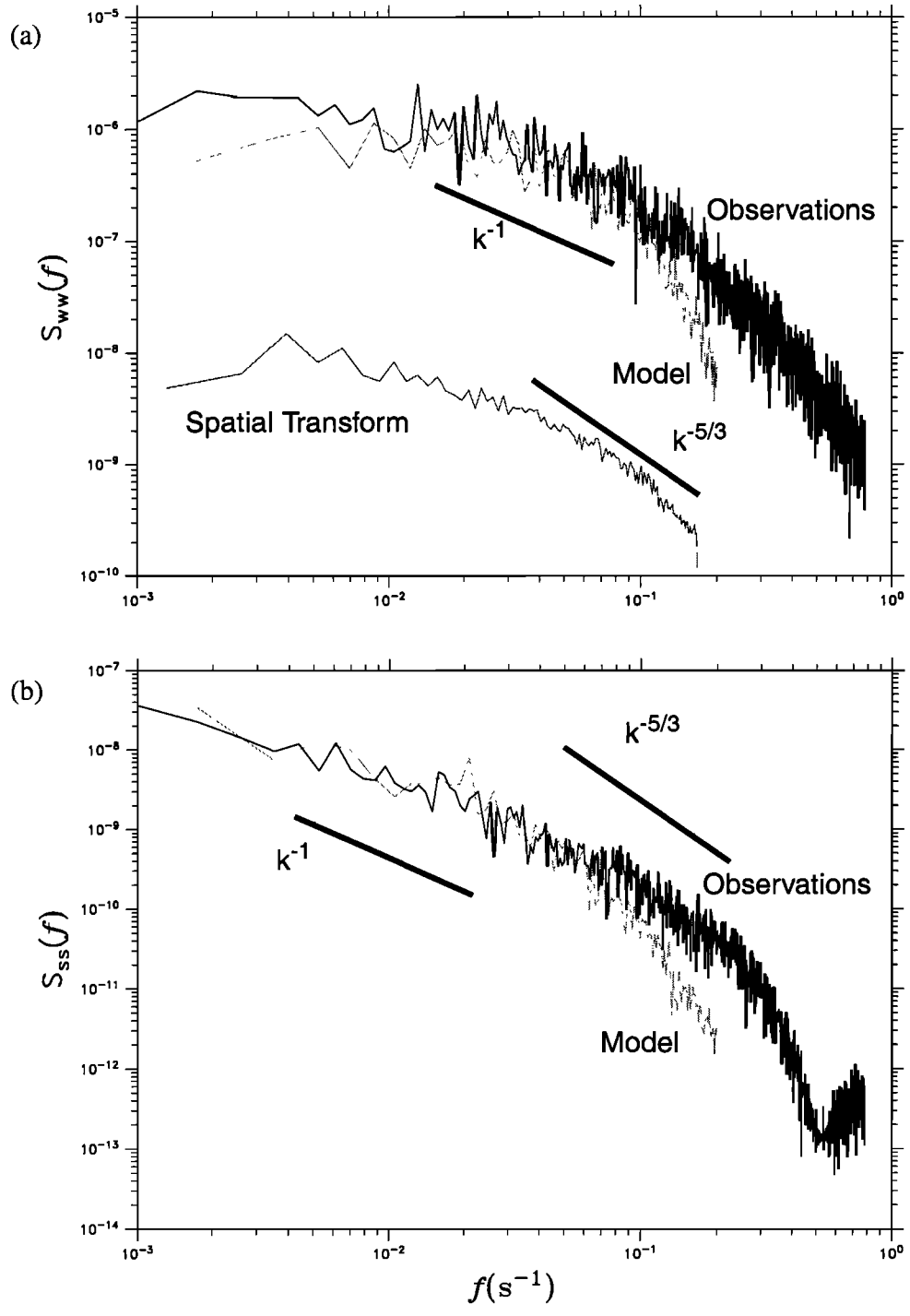

Figure 8. Time series spectra of (a) w and (b) S from LEADEX observations on day 85.122 (black) and model hour 11-12 (gray). Also shown are the $k^{-5/3}$ and k^{-1} spectral curves representing the inertial subrange and production range of turbulence and, in Figure 8a, the model x axis ensemble averaged y axis spectra calculated from hour 12 (labeled "spatial transform").

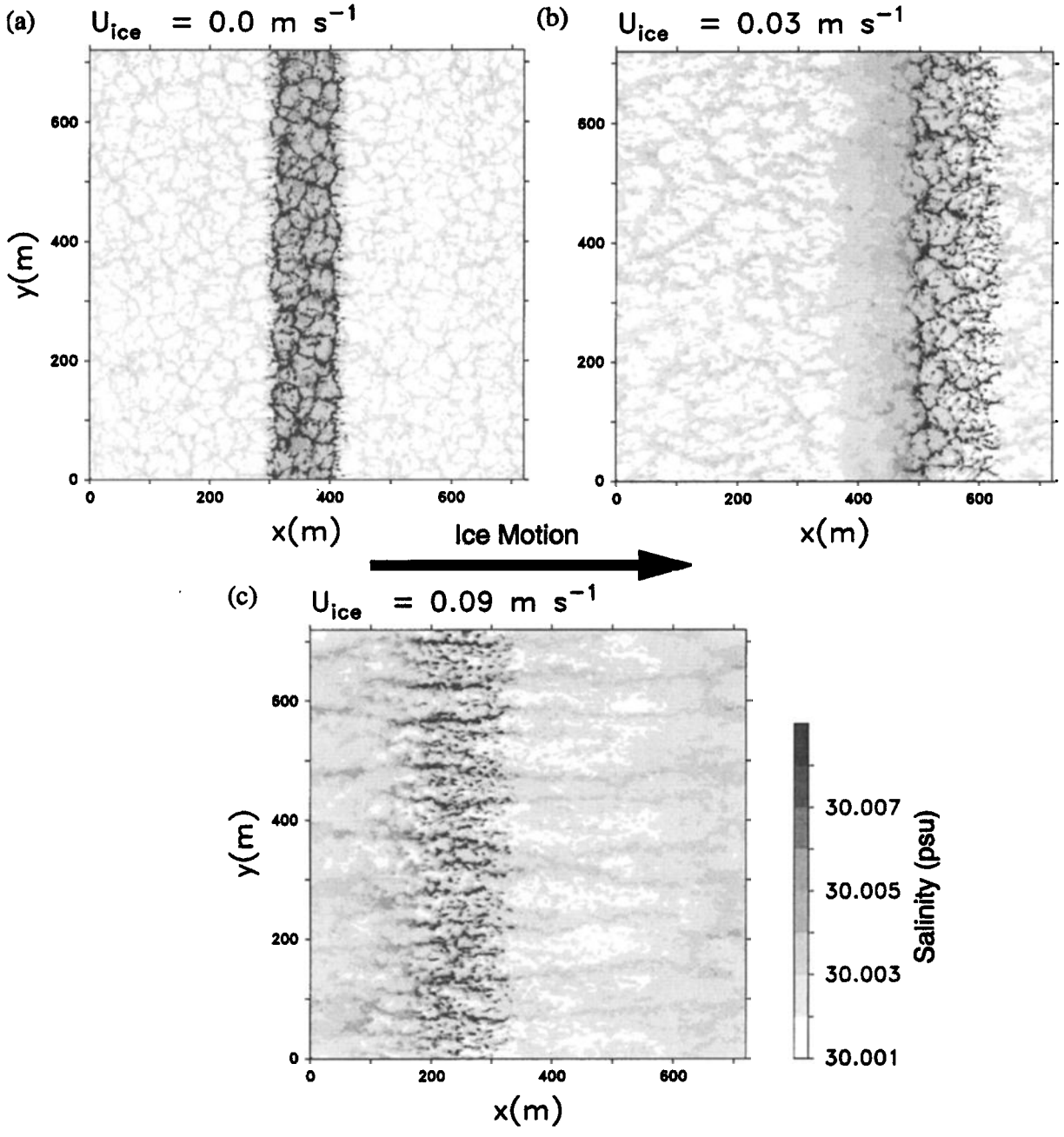

Figure 9. Salinity (psu) at a depth of 3.8 m below the pack ice after 12 hours for ice velocities of (a) 0.0 m s^{-1}, (b) 0.03 m s^{-1}, and (c) 0.09 m s^{-1} and an initial lead width of 150 m. These plots are 2 hours after opening the lead. Note that with U_{ice} = 0.09 m s^{-1} the lead begins at the center of the domain, as in Figure 9a, and advects through the right-hand side periodic boundary, reappearing on the leviathan side and advecting back to almost the middle of the domain, centered at x = ~288 m.

the lead circulation as shown in Figures 9b-9c and 10b. This tends to smooth the effects of lead convection by separating convective elements from the surface forcing and by introducing a diffusive turbulent flux from ice roughness and shear production. The importance of under-ice shear production is made clear by the coherent structure of turbulence within the lead circulation, which is set mostly by streaks that are present under the pack ice. These vortices are enhanced at the lead by increased salinity flux but in general remain coherent as the lead passes overhead. As Figure 10b shows, the enhanced salinity flux at the lead causes a gradual deepening of the saline plumes downstream from the lead. With each plume is a tendency for positive momentum transport as shown by the vector orientation within the plumes. Thus the plumes act to transport mean momentum generated by the ice motion downward into the mixed layer.

Visual inspection of the cross sections shown in Figures 9 and 10 suggests that the vertical salt and heat fluxes beneath leads are greatly affected by increasing ice motion. This is verified by plotting the average salt and heat flux for each

case at hour 12 (Figure 11). In these cases, increasing ice motion forces weaker turbulent heat flux but stronger entrainment at the mixing layer base as indicated by the salinity flux. The depth of the maximum heat flux increases with decreasing ice velocity because individual plumes are able to extend deeper into the boundary layer with less current shear. All of the flux profiles with leads had maxima that were deeper than the no-lead simulations. Plots of the E budget profiles (not presented) are similar to plots for the pack ice simulations shown in Figure 7 but with a stronger buoyancy term because of the increased surface salt flux at the lead.

The relative importance of turbulence generated by ice motion versus buoyancy forcing can be estimated by using the ratio of the mixed layer depth and Monin-Obukhov length scale defined as

$$L_o = \frac{gd(w'\rho')^{\text{lead}}}{\rho(u'w')^{\text{ice}}}, \quad (20)$$

where d = 32 m is the mixed layer depth and the buoyancy and momentum fluxes are estimates over the lead region or pack ice region, respectively. Similar nondimensional numbers are given by *Morison et al.* [1992] and *Kantha* [1995]. Values for L_o range from ~1 for U_{ice} = 0.09 m s^{-1}, indicating a mixed forced and free convection regime, to ~15 for U_{ice} = 0.03 m s^{-1}, implying a free convective scenario. These values are consistent with those reported by *Morison and McPhee* [1998] for leads 3 and 4 of LEADEX, which had ice velocities of ~0.09 and ~0.03 m s^{-1}, respectively.

4.4. Comparison With LEADEX Data From Lead 3

Comparison between LEADEX observations and the model were made by using data from lead 3 taken between day 98.427 and 98.594 at a depth of 4.3 m. At the time of the observations, lead 3 was ~1 km wide, covered with ~8 cm of ice, and had an ice motion of 0.092 m s^{-1}. Time series plots are presented in Figure 12 comparing the observed turbulence characteristics with the model output from the U_{ice} = 0.09 m s^{-1} case. These time series were taken from the downstream lead edge at y = 46.5 m and at a model depth of 3.8 m, using the same x positions as the no-lead case. As in the no-

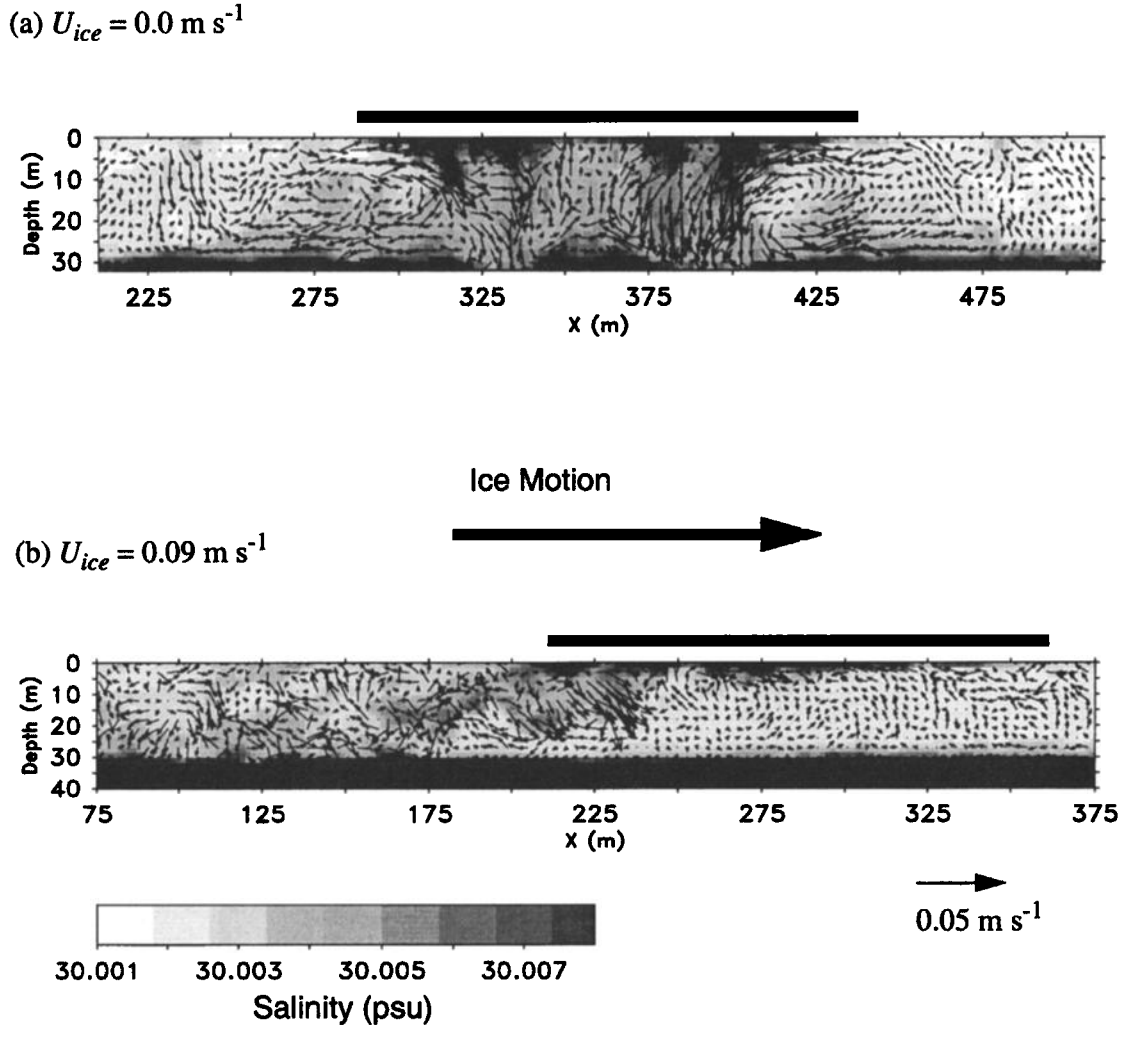

Figure 10. Cross-section plots of salinity and perturbation velocity vector for lead simulations with (a) U_{ice} = 0.0 m s^{-1} and (b) U_{ice} = 0.09 m s^{-1}. Sections are taken from y = 200 at hour 12. Lead position is indicated by the thick line above the plots.

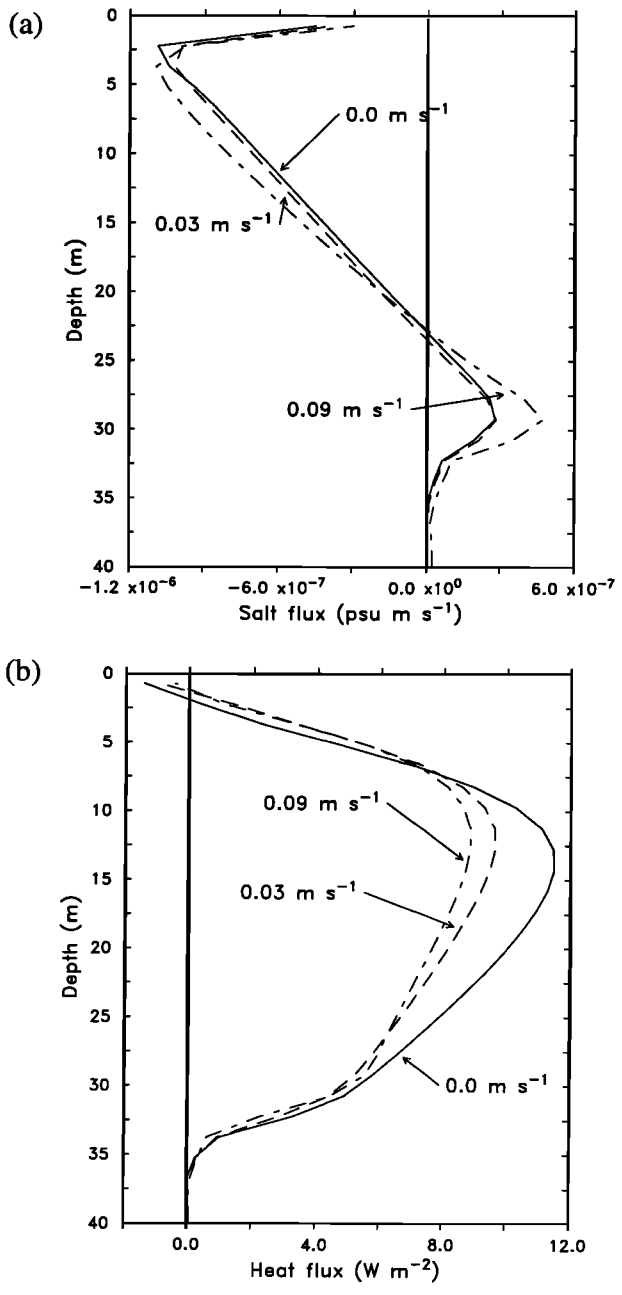

Figure 11. Horizontally averaged (a) salinity flux and (b) heat flux from 150-m lead simulations with ice velocities of 0.0, 0.03, and 0.09 m s^{-1}.

lead case, smoothing in the model causes the greatest qualitative difference between the simulation and measurements. Nonetheless, the model duplicates the general pattern of strong downward moving saline plumes as shown in the LEADEX data. The effect of the lead in these time series is most notable by the much larger temperature and salinity perturbations in comparison with the no-lead case (Figure 7; note the change in axis scales). We also note that perturbations tend to have longer timescales in the lead case, suggesting more coherent plumes of downward moving saline water. There is an indication of ramp-like structures in the time series, with salinity increasing relatively slowly before dropping rapidly as plumes pass the measurement site. They resemble similar structures observed in the atmosphere and OBL, as was noted by *Thorpe* [1985].

Overall, the range of simulated salinity is relatively close to the observations, although temperature variations appear to be greater in the LEADEX data. Heat and salinity flux values show good agreement; however, as Figure 11 shows, vertical turbulent flux gradients vary rapidly near the ice bottom. Thus relatively minor vertical averaging could lead to significant changes in the heat and salinity flux estimates. Plots of the ensemble averaged spectra taken from the five time series cases (Figure 13) also show reasonable correspondence, although the agreement is not a good as the higher-resolution no-lead case (Figure 8). Nevertheless, the spatial spectra still show a region of -5/3 drop-off indicating that the model is simulating a portion of the inertial subrange. The vertical velocity spectra are again in better agreement than the salinity spectra, which shows a "flatter" profile at large scales in comparison with the observations.

The relatively good agreement between the simulated and observed time series and fluxes is somewhat surprising given the much greater lead width for lead 3 versus the model (~1000 m versus 150 m). This can be explained by considering the relatively shallow time series depth relative to the boundary layer changes brought on by the lead surface fluxes. As water passes under the lead, it develops an internal boundary layer forced by the lead surface fluxes. In the time it takes the lead to traverse 150 m, this boundary layer grows to almost the halocline depth at 32 m. Thus the lead internal boundary layer has almost reached the preexisting OBL depth by the time the data are collected. This growth is consistent with *Morison and McPhee* [1998], who used an autonomous underwater vehicle to examine the horizontal turbulent structure beneath lead 3 at 15-m depth, They found that fluxes were relatively uniform across the lead, indicating that the lead-induced boundary layer rapidly reached an equilibrium downstream from the lead edge.

5. Frazil Ice Effects

Although most of the heat lost through the ice goes toward new ice growth at the ice base, a significant fraction of the heat loss acts to cool the ocean just beneath the ice. During LEADEX, the boundary layer temperature structure was typically very near freezing so that heat flux from the water to the ice produced supercooling and formation of frazil ice. Using optical techniques, *Pegau et al.* [1996] observed that most of the frazil ice formed by surface cooling was confined to the upper 2-3 m of the water column. This was also true in our simulations, as is shown by a plot of the y axis averaged frazil ice for the $U_{ice} = 0.09$ m s^{-1} lead case (Figure 14). Modeled concentrations are similar to the observations (~0.05 kg m^{-3}) with the highest concentrations located just beneath the surface and a strong reduction in concentration below ~5 m. Observations of the frazil vertical structure show a sharp cutoff of measurable concentrations between 3- and 4- m depth, whereas in the model, the concentration drops off more smoothly. The frazil model used in the LES only considered a single crystal size and did not simulate the effects of crystal growth. The lack of these processes, along with the coarse grid resolution, could have contributed to the relatively larger concentration in the simulated frazil ice and the greater depth of frazil transport (crystals would have grown and moved upward because of buoyancy). Nevertheless, the simple

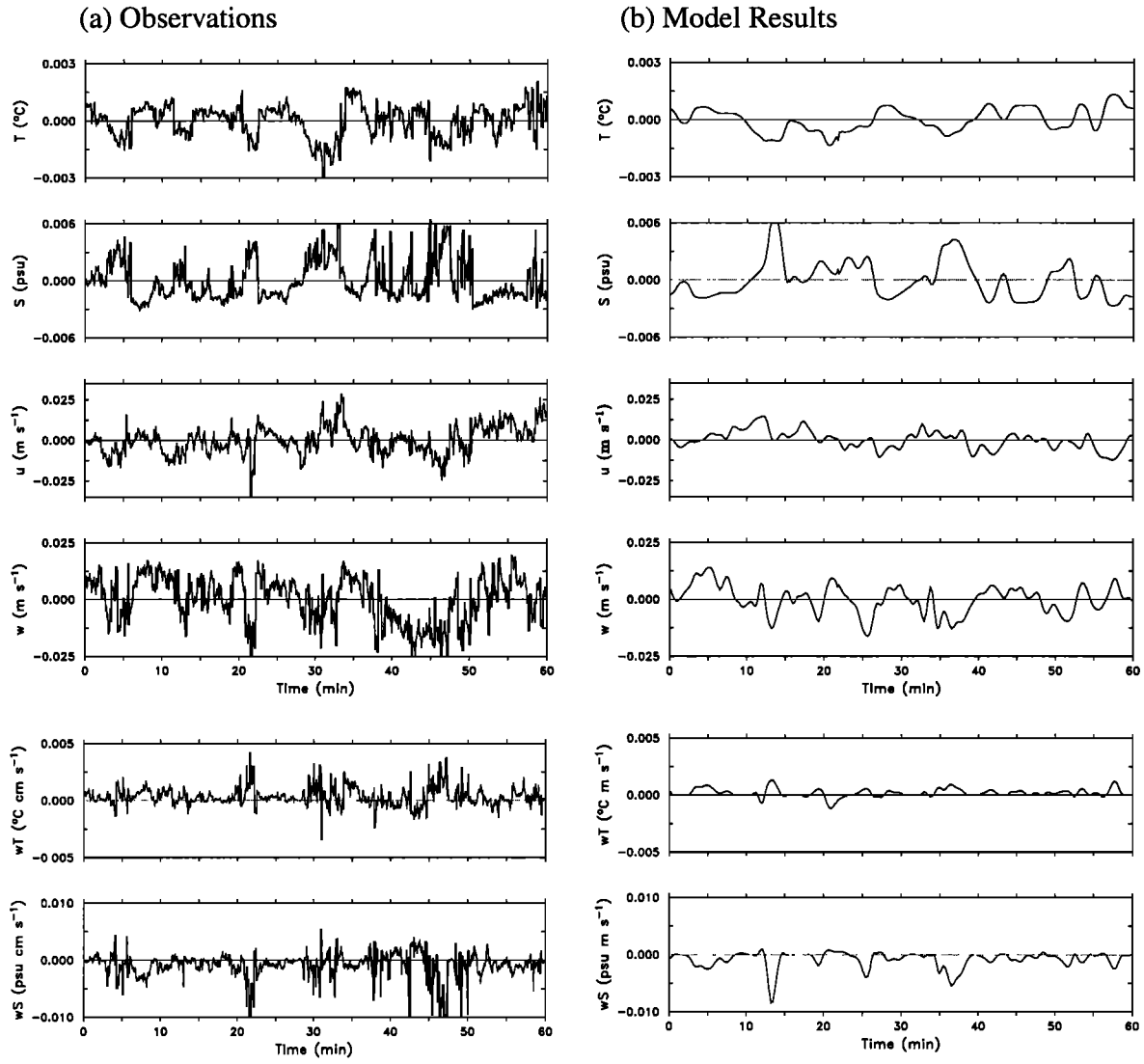

Figure 12. Time series of (a) observed and (b) modeled perturbation temperature, salinity, zonal velocity, vertical velocity, heat flux, and salt flux. Observations are taken from 4.3 m below the ice starting at day 98.51 of LEADEX. Model results are taken between hours 11 and 12 from a depth of 3.8 m on the downstream lead edge at $y = 46.5$ m. The mean observed heat and salinity fluxes are 3.54 x 10^{-6} °C m^{-2} (~14 W m^{-2}) and -1.54 x 10^{-5} psu m s^{-1}, whereas the mean modeled heat and salinity fluxes are ~2.5 x 10^{-6} °C m^{-2} (~10 W m^{-2}) and ~ -1.2 x 10^{-5} psu m s^{-1} (based on five time series adjusted to 4.3 m).

model employed here produced good results for the short time period simulations.

Without frazil ice, the heat budget of the ice-covered boundary layer is incomplete. This is clearly shown by comparing the boundary layer turbulent heat budget with the frazil source term from as presented in Figure 15. Heat flux from the ocean into the ~0.08-m-thick ice over the lead is ~35 W m^{-2} in the simulation. Most of this flux is removed via frazil production in the upper 5 m of the water column as shown by the significant heating generated by frazil production. A large portion of the frazil ice rises to the ice bottom and is incorporated into the ice sheet, effectively decreasing the heat flux out of the upper ocean. Below ~5-m depth, frazil transported downward by turbulence starts to melt as the seawater temperature rises slightly above freezing (because of the pressure effect on freezing point). Melting cools the water column; however, this is offset by turbulent heat transport so that the local temperature change is minor. Frazil concentration falls to near zero below ~10 m, and temperature changes in the lower half of the boundary layer are dominated by cooling from turbulent transport. Continuous cooling of the middepth boundary layer by frazil melting would eventually cause the local temperature to decrease to the freezing point. However, during LEADEX, daytime solar radiation heated the water below the lead with a flux of up to ~100 W m^{-2}, compensating for the nighttime cooling from frazil ice melting.

We note that a similar vertical heating profile is produced by frazil ice in the pack ice simulations discussed in section 1 (not shown). However, in cases with 1-m-thick pack ice, the

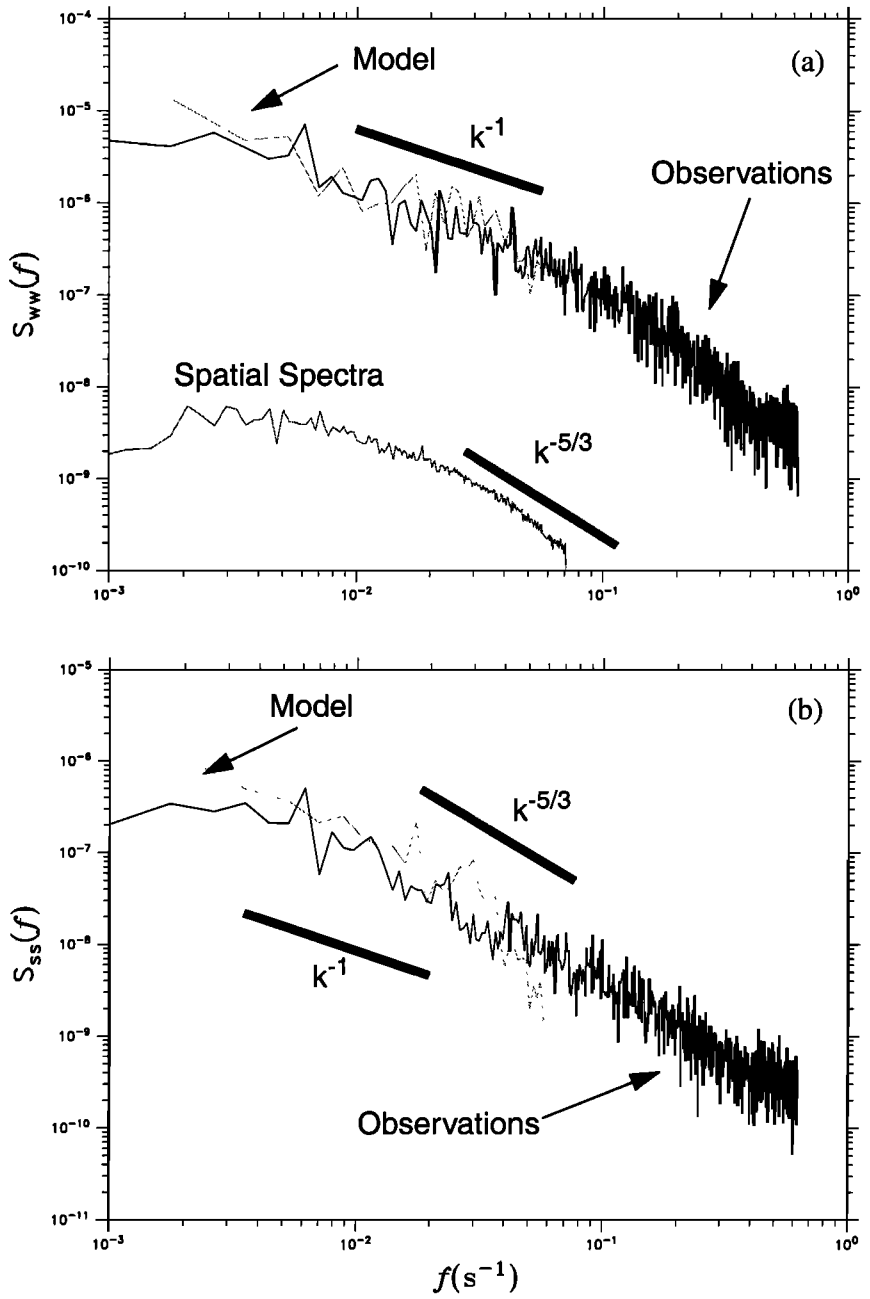

Figure 13. Time series spectra of (a) w and (b) S from LEADEX observations on day 98.51 (black) and model hour 11-12 (gray) from the U_{ice} = 0.09 m s^{-1} lead simulation. The $k^{-5/3}$ and k^{-1} spectral curves are also shown, representing the inertial subrange and production range of turbulence, and the spatial y axis spectra ensemble averaged in the x direction for salinity from z = 3.8 m (offset by a factor of 0.01). Because the frequency spectra are taken from the lead circulation, they have more energy than the spatially averaged spectra.

ocean cooling rates are much smaller, so that frazil concentrations are very small. In addition, most of the frazil ice is deposited on the base of the pack ice before it can be transported to significant depths and melted. Frazil ice in these cases is, in effect, equivalent to an increase in the pack ice freezing rate, which causes less ocean cooling and a greater under-ice salt flux.

A plot of the turbulent heat flux, $w'T'$, averaged along the y axis provides a clearer view of the local effect of the lead (Figure 16). Beneath the lead, heat flux is relatively small, as most of the surface heat loss goes toward frazil ice formation. As the frazil ice melts and plume velocities increase downstream from the lead, the turbulent heat flux increases to a maximum ~25-50 m downstream from the lead edge. The local maximum in heat flux decreases to near background values ~200 m downstream from the lead.

The vertical profile of heat flux in Figure 16 at the downstream lead edge is consistent with LEADEX measurements,

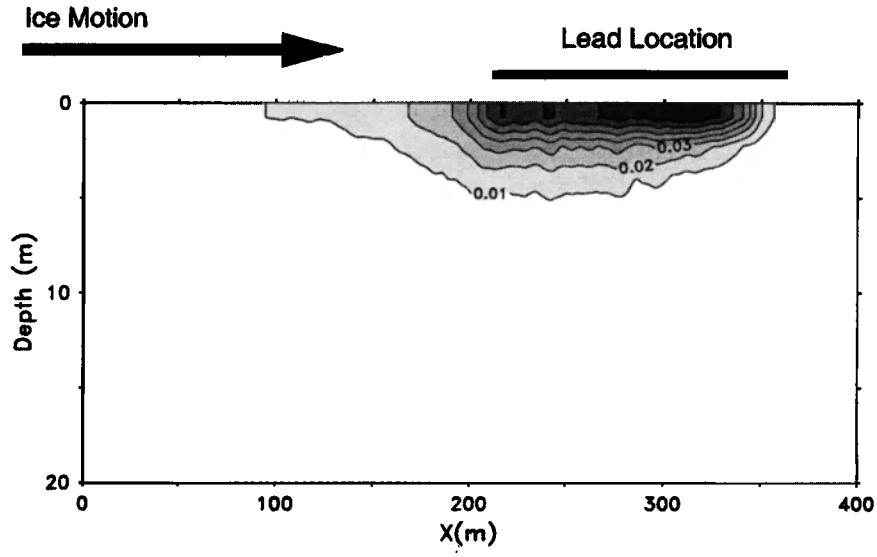

Figure 14. Cross section of y axis averaged frazil ice concentration in kg m^{-3} at hour 12 for the U_{ice} = 0.09 m s^{-1} lead simulation.

showing an increase from ~6 W m^{-2} at 4-m depth to ~30 W m^{-2} at 10-m depth reported in MS. Without frazil ice, it is difficult to explain how heat flux would increase with depth below the lead at night. Typical boundary layer heat flux profiles for a cooled convective boundary layer show a maximum in turbulent heat flux just below the surface and a near-linear decrease in heat flux with depth [see *Skyllingstad and Denbo*, 1995]. One alternative explanation for the heat flux maximum might be the entrainment of relatively warm water from the pycnocline (since water temperature increases with increasing depth). This is evident in Figure 16, as is shown by the higher heat flux at ~30 m. However, fluxes related to entrainment cover a smaller region and are physically separate from the maximum heat flux in the middle of the boundary layer downstream from the lead. Because most of the downward shift in heat flux is due to frazil ice effects, we believe the role of frazil ice may be critical in determining the polar ocean heat budget, especially under leads.

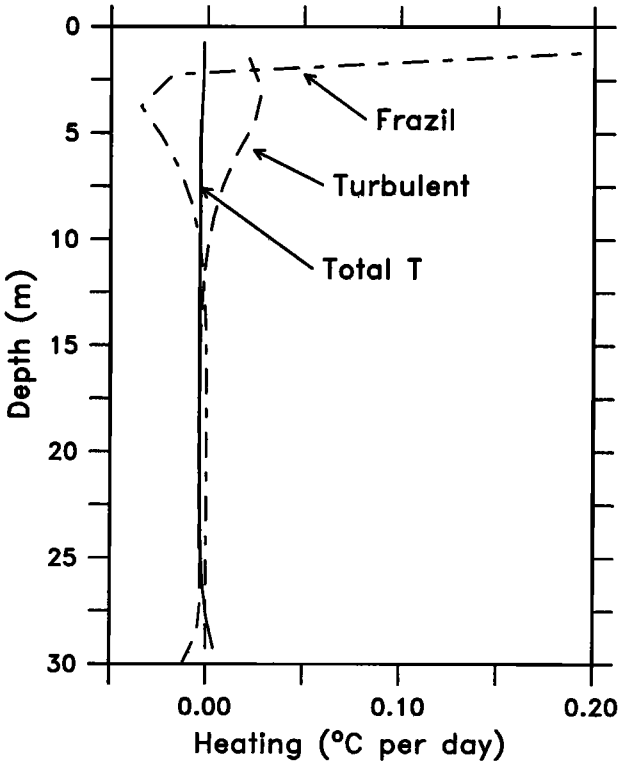

Figure 15. Total heating rate for U_{ice} = 0.09 m s^{-1} lead simulation along with turbulent flux and frazil heating rates averaged between hours 10 and 12. Note that most of the frazil heating above ~ 4 m is accounted for by deposition of frazil ice on the bottom of the surface ice slab.

6. Conclusions

A large-eddy simulation of turbulence under freezing sea ice and leads was performed for a range of ice velocities and compared with observed turbulence parameters. Stationary ice without leads produced turbulent structures that exhibited a cellular pattern similar to atmospheric boundary layer convection noted in previous LES studies. Ice motion caused this pattern to break down rapidly, with ice velocities as low as 0.03 m s^{-1} promoting the formation of streak-like structures aligned with the ice motion. With increasing ice velocity, the horizontal separation between the streaks grew, and they became less distinct because of more vigorous small-scale turbulence. Analysis of the heat and salinity fluxes showed that slow-moving ice caused a decrease in the relative strength of the heat flux just under the ice relative to stationary ice, but with faster velocity, the flux again increased. Entrainment at the mixed layer base also increased in response to shear generated by more boundary layer momentum. Analysis of the TKE budget for each case demonstrated how shear production from strong ice velocities overwhelmed entrainment from negatively buoyant plumes in the stationary case.

Opening of leads caused significant changes in the turbulent structure of the mixed layer, particularly when ice veloc-

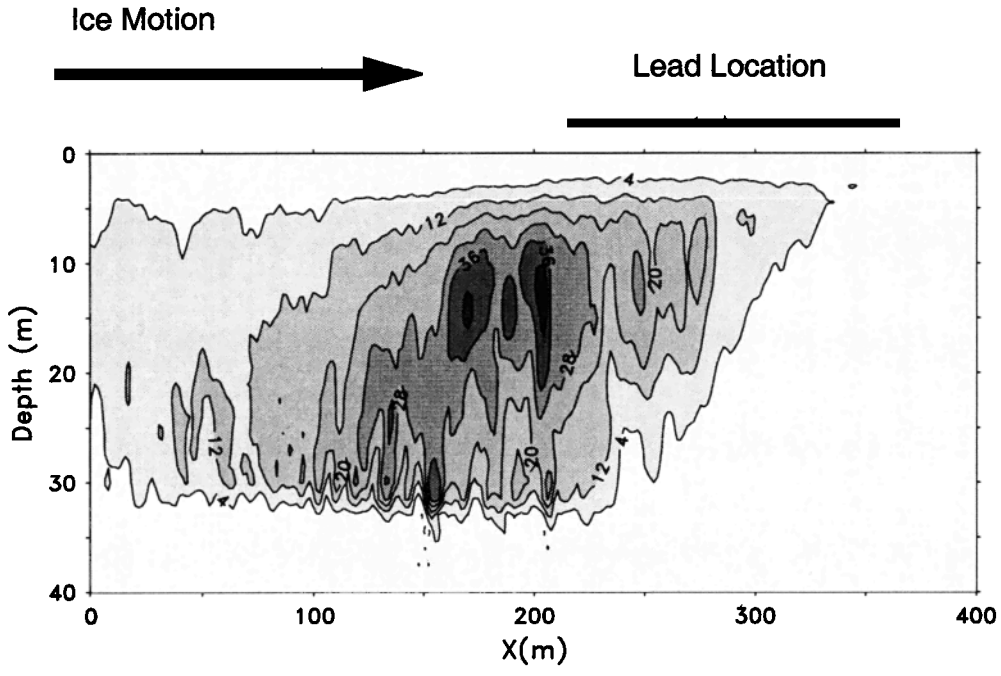

Figure 16. Cross section of turbulent heat flux ($\rho C_p w'T'$) from the $U_{ice} = 0.09$ lead case at hour 7. The heat flux is averaged along the y axis. Thick line above the graph signifies the approximate location of the lead.

ity was small. A 150-m lead in stationary ice generated two downwelling regions with spacing of ~50 m, centered in the middle of the lead. Ice motion caused a much different structure, with preexisting coherent streak structures defining the main plumes of higher-salinity water beneath the lead. Traveling leads produced a trailing plume of enhanced salinity and downward directed velocity that lengthened with increasing ice velocity. In comparison with the pack ice simulations, heat flux peaked at greater depths because of the higher concentration of frazil ice and related heat transport.

Model time series data taken from a point moving with the ice showed good comparison with LEADEX data from under pack ice and the edge of a 1-km-wide lead. Qualitative comparison showed that the model was able to duplicate low-frequency flow features, such as plume structures, with good accuracy. Comparison of modeled and measured vertical velocity and salinity spectra showed good agreement at low frequencies covering a portion of the production range and inertial subrange.

Fluxes were also modeled accurately; however, this good agreement was partly a result of the ice crystal size selection in the frazil ice model. Nevertheless, the constant frazil ice crystal size yielded good results for very different forcing scenarios (i.e., under 1-m-thick ice versus 0.08-m lead ice), indicating that the model is robust and should be applicable over a range of conditions. Transport of heat by frazil ice in the boundary layer was found to have a significant role in determining the overall flux of heat into the upper ocean. Near the ice bottom, most of the heat transferred to the water was used to form frazil ice, which was then deposited under the ice and mixed downward by turbulence. Melting of the transported frazil caused cooling of the upper boundary layer water and a corresponding increase in the local turbulent heat flux. As a result, turbulent heat flux was found to increase with depth and have a maximum at about the middle of the boundary layer. In comparison, typical convective boundary layers have a maximum turbulent flux just below the cooled surface [e.g., *Skyllingstad and Denbo,* 1995]. A possible consequence of this result is that accurate measurements of under-ice heat flux may require turbulence measurements away from the ice bottom to avoid errors associated with latent heat contained in transported frazil ice.

Simulation results imply that the effect of leads on the upper ocean heat and salinity budgets may need specialized parameterization in models of the polar oceans. For example, our results indicate that frazil ice under leads can carry a significant heat flux (i.e., ~10-30 W m^{-2}) and needs to be represented in the upper ocean heat budget. Most thermodynamic sea ice models simply convert all heat into new ice when the ocean temperature reaches the freezing point. LEADEX measurements and our results indicate that a significant fraction of the outgoing heat flux can cool the ocean boundary layer while ice is forming. We plan to further explore this hypothesis in future research by using data from the Surface Heat Budget in the Arctic (SHEBA) experiment.

Acknowledgments. The authors would like to thank the three anonymous reviewers and William Smyth and Clayton Paulson for very useful comments. Special gratitude is extended to Miles McPhee for kindly supplying turbulence data from LEADEX. We would also like to acknowledge the supercomputer time provided by the National Center for Atmospheric Research. This work was supported as part of the SHEBA project by National Science Foundation grant OCE-97-03539.

References

Backhaus, J. O., and J. Kämpf, Simulations of sub-mesoscale oceanic convection and ice-ocean interactions in the Greenland Sea, *Deep Sea Res., Part II, 46,* 1427-1455, 1999.

Cox, G. F. N., and W. F. Weeks, Numerical simulations of the profile of undeformed first-year sea ice during the growth season, *J. Geophys. Res.*, *93*, 12,449-12,460, 1988.

Denbo, D. W., and E. D. Skyllingstad, An ocean large-eddy simulation model with application to deep convection in the Greenland Sea, *J. Geophys. Res.*, *101*, 1095-1110, 1996.

Ebert, E. E., and J. A. Curry, An intermediate one-dimensional thermodynamic sea ice model for investigating ice-atmosphere interactions, *J. Geophys. Res.*, *98*, 10,085-10,109, 1993.

Eicken, H., et al., Ice-tank studies of physical and biological sea-ice processes, in *Ice in Surface Waters*, edited by H. Shen, pp. 363-370, A. A. Balkema, Brookfield, Vt., 1998.

Jenkins, A., and A. Bombosch, Modeling the effects of frazil ice crystals on the dynamics and thermodynamics of ice shelf water plumes, *J. Geophys. Res.*, *100*, 6967-6981, 1995.

Kader, G. G., and A. M. Yaglom, Spectra and correlation functions of surface layer atmospheric turbulence in unstable thermal stratification, *Turbulence and Coherent Structures*, edited by O. Metais, 450 pp., Kluwer Acad., Norwell, Mass., 1991.

Kämpf, J., and J. O. Backhaus, Ice-ocean interactions during shallow convection under conditions of steady winds: Three-dimensional numerical studies, *Deep-Sea Res., Part II*, *46*, 1335-1355, 1999.

Kantha, L. H., A numerical model of Arctic leads, *J. Geophys. Res.*, *100*, 4653-4672, 1995.

Katul, G. G., and M. B. Parlange, The spatial structure of turbulence at production wavenumbers using orthonormal wavelets, *Boundary Layer Meteorol.*, *75*, 81-108, 1995.

Khanna, S., and J. G. Brasseur, Three-dimensional buoyancy- and shear-induced local structure, *J. Atmos. Sci.*, *55*, 710-743, 1998.

Klemp, J. B., and D. R. Durran, An upper boundary condition permitting internal gravity wave radiation in numerical mesoscale models, *Mon. Weather Rev.*, *111*, 430-445, 1983.

Levine, M. D., C. A. Paulson, J. Simpkins, and S. R. Gard, Observations from LEADEX, Beaufort Sea Arctic Ocean, March-April, 1992, *COAS Data Rep. 153*, 160 pp., Oreg. State Univ., Corvallis, 1993.

Mason, P. J., Large eddy simulation of the convective atmospheric boundary layer, *J. Atmos. Sci.*, *46*, 1492-1516, 1989.

Maykut, G. A., Energy exchange over young sea ice in the central Arctic, *J. Geophys. Res.*, *83*, 3646-3658, 1978.

McPhee, M. G., Turbulent heat flux in the upper ocean under sea ice, *J. Geophys. Res.*, *97*, 5365-5379, 1992.

McPhee, M. G., and T. P. Stanton, Turbulence in the statically unstable oceanic boundary layer under Arctic leads, *J. Geophys. Res.*, *101*, 6409-6428, 1996.

McPhee, M. G., G. A. Maykut, and J. H. Morison, Dynamics and thermodynamics of the ice/upper ocean system in the marginal ice zone of the Greenland Sea, *J. Geophys. Res.*, *92*, 7017-7031, 1987.

Mellor, G. L., M. G. McPhee, and M. Steele, Ice-seawater turbulent boundary layer interaction with melting or freezing, *J. Phys. Oceanogr.*, *16*, 1829-1846, 1986.

Moeng, C.-H., A large-eddy simulation for the study of planetary boundary layer turbulence, *J. Atmos. Sci.*, *41*, 2052-2062, 1984.

Moeng, C.-H., and P. P. Sullivan, A comparison of shear and buoyancy driven planetary boundary layer flows. *J. Atmos. Sci.*, *51*, 999-1022, 1994.

Morison, J. H., and M. G. McPhee, Lead convection measured with an autonomous underwater vehicle, *J. Geophys. Res.*, *103*, 3257-3281, 1998.

Morison, J. H., M. G. McPhee, T. B. Curtin, and C. A. Paulson, The oceanography of winter leads, *J. Geophys. Res.*, *97*, 11,199-11,218, 1992.

Omstedt, A., and U. Svensson, Modeling supercooling and ice formation in a turbulent Ekman layer, *J. Geophys. Res.*, *89*, 735-744, 1984.

Pegau, W. S., C. A. Paulson, and J. R. V. Zaneveld, Optical measurements of frazil concentration, *Cold Reg. Sci. Technol.*, *24*, 341-353, 1996.

Skyllingstad, E. D., and D. W. Denbo, An ocean large-eddy simulation of Langmuir circulations and convection in the surface mixed layer, *J.Geophys. Res.*, *100*, 8501-8522, 1995.

Skyllingstad, E. D., W. D. Smyth, J. N. Moum, and H. Wijesekera, Upper ocean turbulence during a westerly wind burst: A comparison of large-eddy simulation results and microstructure measurements. *J. Phys. Oceanogr.*, *29*, 5-28, 1999.

Skyllingstad, E. D., W. D. Smyth, and G. B. Crawford, Resonant wind-driven mixing in the ocean boundary layer, *J. Phys. Oceanogr.*, *30*, 1866-1890, 2000.

Smith, D. C., IV, and J. H. Morison, A numerical study of haline convection beneath leads in sea ice, *J. Geophys. Res.*, *98*, 10,069-10,087, 1993.

Smith, D. C., and J. H. Morison, Nonhydrostatic haline convection under leads in sea ice. *J. Geophys. Res.*, *103*, 3233-3247, 1998.

Thorpe, S. A., Small-scale processes in the upper ocean boundary layer, *Nature*, *318*, 519-522, 1985.

United Nations Educational, Scientific, and Cultural Organization, Tenth report on the Joint Panel of Oceanographic Tables and Standards (1981). UNESCO Tech. Pap. in Mar. Sci. No. 30, Paris, 1981.

Yaglom, A. M., and B. A. Kader, Heat and mass transfer between a rough wall and turbulent fluid flow at high Reynolds and Peclet numbers, *J. Fluid Mech.*, *62*, 601-623, 1974.

D.W. Denbo, Joint Institute for the Study of the Atmosphere and Ocean, University of Washington, NOAA/PMEL/OC, 7600 Sand Point Way NE, Seattle, WA, 98115. (dwd@pmel.noaa.gov)

E.D. Skyllingstad, 104 Ocean Administration Building, Oregon State University, Corvallis, OR, 97331. (skylling@oce.orst.edu)

(Received October 11, 1999; revised May 26, 2000; accepted October 10, 2000.)